Computational library for the Nutrient-Unicellular-Multicellular plankton modeling framework v. 1.0

Amalia Papapostolou[1], Anton V. Almgren[1], Trine F. Hansen[1], Athanasios Kandylas[1], Camila Serra-Pompei[1], Andre W. Visser[1], and Ken H. Andersen[1]

[1]Center for Ocean Life, Natl. Institute for aquatic resources, Technical University of Denmark

Correspondence to: Amalia Papapostolou (ampap@dtu.dk)

Abstract. The Nutrient-Unicellular-Multicellular (NUM) model is a trait-based model of unicellular and multicellular plankton that uses body size as the main structuring variable for community composition. The distinguishing feature is that body size is used for structuring predator-prey interactions and to scale all parameters. For unicellular plankton, trophic strategies across the full range from osmotrophy, phototrophy, phagotrophy and mixotrophy, are an emergent outcome of the model. Another distinguishing feature is that the multicellular component, represented by copepods, includes ontogeny, which is crucial in shaping population dynamics. In addition, the framework encompasses a nutrient pool consisting of nitrogen, silica and dissolved organic carbon (DOC) which interacts dynamically with the plankton community in three model setups: a chemostat simulating the photic zone, a water-column, and a global setup. Here we present a user-friendly Fortran-Matlab library which makes the NUM model accessible as a practical tool for marine ecologists or biogeochemical modellers. The model output is validated with *in situ* and satellite data and demonstrates its applicability in chemostat, water-column, and global setups.

1 Introduction

Marine planktonic food webs play an important role in the ocean's biogeochemical cycles, influence the Earth's climate regula-
tion, and determine potential fisheries yields (Stock et al., 2014). Plankton participate in the global carbon cycle by accounting
for roughly half the global carbon fixation through photosynthesis, and by sequestering carbon via sinking dead detrital mat-
ter (Basu and Mackey, 2018; Boyd et al., 2019). The production of new biomass from photosynthesis also determines the
amount of carbon available to higher trophic levels of fish production, which globally support about 17% of human protein
consumption (Waite et al., 2014).

Current Earth system models of the planktonic food web focus on phytoplankton, because these organisms directly drive
photosynthesis and their fast turnover rates mean that they have the highest loss rates to the biological carbon pump. Other
plankton groups are represented by predatory zooplankton, which often mainly act as a closure term on the phytoplankton.
This representation of the planktonic food web as phytoplankton and zooplankton has three shortcomings: First, it is becoming
increasingly clear that higher trophic level organisms, in particular multicellular plankton dominated by copepods, also affect
the biological carbon pump (Steinberg and Landry, 2017; Serra-Pompei et al., 2021). While their turn-over rates are much
slower than phytoplankton, they produce fast-sinking fecal pellets that sink to the deep ocean before they are remineralized
(Turner, 2015; Nowicki et al., 2022). Second, potential fishery production is not directly determined by phytoplankton produc-
tion –fish are generally too large to consume phytoplankton. Instead, it is determined by the production of copepods and other
multicellular zooplankton (Mitra et al., 2014; Castonguay et al., 2008). This production in turn depends on the structure of the
unicellular plankton food chain, in particular upon whether the primary producers are dominated by small bacteria or large
diatoms (Vargas et al., 2006; Brett et al., 2009; Boyce et al., 2015). Third, the paradigm of plankton being well represented
as either phytoplankton (plants) or zooplankton (animals) has been broken by the realization that most eukaryotic plankton
are neither phytoplankton or zooplankton but mixotrophic jacks-of-all-trades to various degrees (Millette et al., 2023). Re-
solving mixotrophy leads to a more realistic representation of the plankton dynamics (Flynn et al., 2013) and weighs heavily
in calculating correctly the trophic efficiency of the primary production towards fish (Ward and Follows, 2016). Taken to-
gether, a sufficient representation of the functions of marine planktonic food webs regarding climate regulation and potential
fisheries production requires a representation of the mixotrophic nature of eukaryotic plankton as well as a representation of
multicellular plankton, in particular copepods.

Current plankton models introduce additional complexity by splitting phyto- and zooplankton into further functional groups
(Fasham et al., 1990). This strategy has been successfully applied in regional ecosystems where the parameters for each
functional group can be tuned to represent the dominant species in the examined region (Turner et al., 2014). However, for
global applications or for applications of environmental change where the dominant species may change, the functional group
model may be driven outside its calibration envelope. An alternative approach has been to eschew functional groups entirely
and only represent differences between plankton organisms by their dominant trait, namely their size (cell size or body size)
(e.g. Ward and Follows, 2016; Chakraborty et al., 2020; Andersen and Visser, 2023; Hansen et al., 2024). Nevertheless, while
size is indeed the "master" trait (Andersen et al., 2016), the pure size-based representation ignores key functional groups such

as diatoms (Cadier et al., 2020). Therefore, plankton models generally adopt a mixture of size-based and functional-group type of models (Stock et al., 2014; Ward et al., 2018; Follows et al., 2007).

The inclusion of realistic representations of multicellular plankton still remains rare (but see Record et al., 2013) for two reasons: First, multicellular zooplankton can increase several orders of magnitude in body mass from eggs to adults, with a growth rate which depends on the availability of food, among other factors. Representing multiple stages requires several state variables to represent just one species. Second, copepod diversity varies strikingly in different regions (Rombouts et al., 2009) and representing all dominant species in global models is not feasible. The Nutrient-Unicellular-Multicellular (NUM) model solves the first problem by using an efficient representation of life history as a physiologically structured model (De Roos et al., 2008) and the latter problem by describing the diversity of copepods by two traits: their adult body size and their feeding mode (passive or active) (Serra-Pompei et al., 2020). Here we build upon this model framework.

A central aim of the NUM model is to base all parameters on first principles, thereby avoiding free parameters that require calibration.

A final scientific challenge is the technical difficulty and the computational time for executing global simulations of full plankton ecosystem models. To enable marine ecologists who without expertise in global biogeochemical modelling to perform global simulations, we introduce the NUM model library version 1.0. The library is based on the NUM model as described in Serra-Pompei et al. (2020) and Serra-Pompei et al. (2022) with a number of key additions: 1) the inclusion of an explicit diatom functional group and silicate dynamics; 2) inclusion of labile dissolved organic carbon and (emergent) heterotrophic bacteria; 3) emergent respiration of unicellular plankton due to uptake regulation; 4) a fast Fortran implementation of the core functions; 5) a matlab front-end with three model setups: chemostat, water column, and global; 6) a flexible configuration of plankton communities, ranging from single group (e.g. unicellular plankton) to a full setup with unicellular generalists (including osmotrophs, phototrophs, and phagotrophs, and mixotrophs), diatoms, sinking particular organic matter, and a complete representation of the multicellular copepod community.

In the following, we first provide an overview of the NUM model structure and implementation, followed by a description of the key equations in the model. Next, we compile global validation data and compare it with global model simulations. Finally, we present examples of the model output, from global patterns to cell-level metabolism, and discuss open issues and potential applications of the NUM library.

2 The Nutrient-Unicellular-Multicellular library version 1.0

The core of the NUM model consists of a set of coupled ordinary differential equations for the state variables. These equations are all coded in a Fortran library for computational efficiency, while the code is executed from a matlab interface. The equations require a representation of the physical environment, which could be a regional circulation model (Hansen et al., 2024) or a simple chemostat (Andersen and Visser, 2023). The matlab front-end to the Fortran library, interfaces with three environments: a chemostat, a water-column, and the entire globe. All the setups are derived from a global transport matrix (Fig. 1a). The
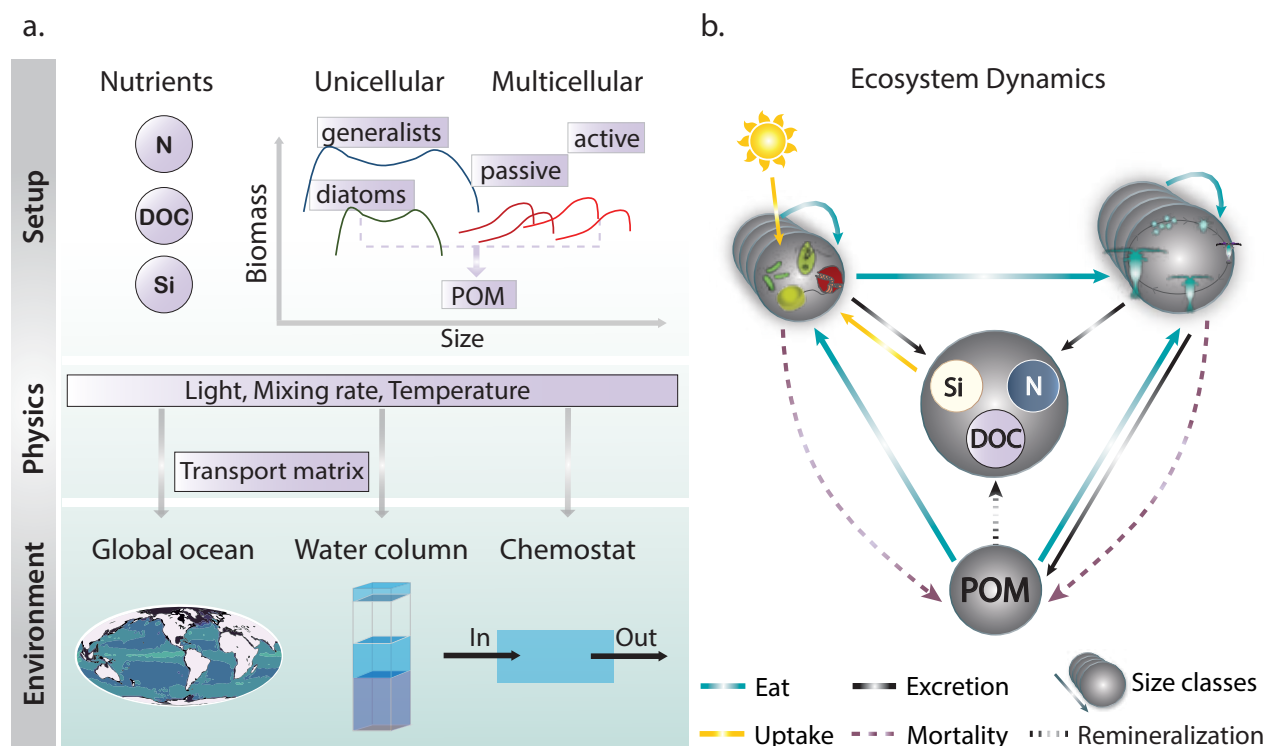
Figure 1. Conceptual sketch of the NUM framework. Panel (a) illustrates the ecological setup and the coupling to physical environments. Panel (b) describes the ecosystem dynamics. Several size-classes are modeled in each plankton group. The number of size classes and plankton groups can be defined at the beginning of each model run.

combination of computationally efficient compiled code with an interpreted language allows to run global simulations on a
80 standard laptop.

The NUM state variables belong to one of three groups: biogeochemical tracers (referred to as "nutrients", including dissolved organic carbon DOC, nitrogen, and silicate), unicellular plankton (generalists or diatoms), and multicellular zooplankton groups (copepods) (Fig. 1b). The unicellular and multicellular groups are represented by "size spectra" encompassing a number of state variables that each models the dynamics of one size group (Fig. 1a). By implementing several sizes of the unicellular
85 and multicellular groups, the size spectrum of the entire plankton community emerges. Size – defined as cell size of unicellular organisms and body size of multicellular organisms– is the key trait that describes resource encounter and uptake, as well as the physiology of individual plankton organisms (metabolism, growth, and reproduction) (Hillebrand et al., 2022). Further, size determines the central process in the model, which is predation by larger organisms on smaller ones (Wirtz, 2012). By using size as the core structuring variable, each organism group is described by one set of parameters defined through size scalings.
90 This approach reduces the overall number of parameters and permits a flexible number of state variables.

The four size spectrum groups described below are generalists, diatoms, copepods, and dead particulate organic matter (POM).

2.0.1 Unicellular generalists

The "generalist" group represents all unicellular plankton including bacteria, phytoplankton, phagotrophs, and mixotrophs
95 (organisms which combine trophic strategies, such as photosynthesis, diffusive uptake of nutrients and predation on smaller cells). This group represents all unicellular plankton (heterotrophic and photosynthetic bacteria, flagellates, dinoflagellates, ciliates, etc.) except diatoms, which we simulate as a separate group (explained in the following section). The generalists are all modelled as mixotrophs that acquire carbon through a combination of osmotrophy (taking up dissolve organic carbon), autotrophy (photosynthesis), and/or phagotrophy. Whether a given size group represents bacteria, phytoplankton, etc., depends
100 on the principal mode of carbon acquisition , which is determined by a combination of cell size and the environment. The trophic strategies of each size class is therefore an emergent property and varies dynamically over space and time. The generalist spectrum is thus a trait-based model with cell size being the trait.

2.0.2 Diatoms

Diatoms are simulated as a separate group because of their importance in marine systems (they account for about 40% of
105 marine primary production (Tréguer et al., 2018)), and their distinct characteristics that affect their physiology and predation mortality. Diatoms enclose a vacuole that increases their volume, allowing them to have larger physical size than other cells of the same biomass. This trait allows them to increase their volume per carbon without additional nutrient demands, which in turn leads to lowered predation pressure, since predation mortality generally decreases with volume (Kiørboe and Hirst, 2014; Thingstad et al., 2005). The vacuole requires a silica shell. The rigidity of the hard silica shell deprives the cell of the
110 plasticity needed to engulf prey and excludes diatoms from eating prey. Diatoms are therefore obligate phototrophs. Moreover, the hard silica shell further lowers the predation pressure on the diatoms (Hamm et al., 2003). Lastly, large diatoms, that thrive in eutrophic environments, have historically been correlated with food webs that lead to major fisheries (Ryther, 1969). Thus, the inclusion of diatoms in the model is critical for the estimation of fish production potential.

2.0.3 Copepods

115 Multicellular zooplankton are the key link between lower and higher trophic levels, as they ingest unicellular plankton and are themselves prey for fish. Among the different zooplankton taxa in the ocean, copepods are the most abundant metazoans (Humes, 1994). Copepods undergo size changes throughout their life stages and thereby occupy different ecological niches. These ontogenetic niche shifts substantially impact population dynamics (Verity and Smetacek, 1996). For instance, copepod growth rates are strongly correlated with spring bloom intensity (Durbin and Durbin, 1992). In particular, spring blooms are
120 controlled by a time lag between the maximum consumption by adult copepods and the rise of juveniles (Vidal and Smith,

1986). To account for these size changes, each population of copepods is represented by a size spectrum that spans from the offspring size to the adult size.

Each population of copepods is characterized by two traits: the adult size and their feeding strategy (active or passive). Modelling the diversity of copepods with these two main traits makes it possible to represent the entire copepod community in the global ocean with just a few representative populations.

2.0.4 Particulate organic matter

Dead organic matter (detritus) is represented by a size spectrum of particulate organic matter (POM) that includes dead organisms, cell fragments from lysis, and fecal pellets from multicellular plankton. POM is represented by a size spectrum to enable the calculation of sinking velocities for different POM sizes. However, in the simulations presented here we have used a single POM group.

3 Model description

Here we describe the main processes in the NUM model. We first describe the size-based predation among modelled organisms and by larger organisms outside the model. Then we describe the cell model (generalists and diatoms), the multicellular model, the POM model, and the biogeochemical model (Fig. 1). The full equations for each model component are given in the supplementary material (App. B).

3.1 Predation

Predation is the central process that connects the plankton size classes in NUM. Each size class i is characterized by its mass m_i (either cell mass or body mass in μg carbon) and the organisms in the class prey on smaller organisms m_{prey} with a log-normal preference function:

$$\phi_{kl}(m, m_{\text{prey}}) = p_{kl} \exp\left[-\frac{\ln^2\left(\frac{m}{\beta_k m_{\text{prey}}}\right)}{2\sigma_k^2}\right], \tag{1}$$

where β is the preferred predator:prey mass ratio, σ is the width, and p_{kl} is the preference of the predator group k towards the prey group l (all parameters are given in Tables B2, B1, B3, and B5 in the supplementary). As each size class represents a finite range of sizes (with m representing the geometric mean; see Fig. C1), the actual preference is the average of the encounter over all prey and predator masses, so the average encounter θ_{ij} between two size classes i (predator) and j (prey) becomes a more complex function (App. D).

The available food for size class i is the sum over all other size classes weighted by the preference (θ_{ij}): $F_i = \sum_i \theta_{ij} B_j$ where B_j is the biomass concentration of prey (μg C L^{-1}). The actual consumption is limited by a maximum mass-specific maximum consumption rate: j_{Fmax} (day^{-1}):

$$j_{\text{F}.i} = \epsilon_{\text{F}} f_i j_{\text{Fmax}.i} \quad \text{with} \quad f_i = \frac{a_{\text{F}.i} F_i}{a_{\text{F}.i} F_i + j_{\text{Fmax}.i}}, \tag{2}$$

where $a_{\mathrm{F},i}$ is the mass-specific clearance rate of the predator ($\mathrm{L}(\mu\mathrm{g\ C\ day})^{-1}$) and ϵ_F is the assimilation efficiency. The predation results in a predation mortality on the prey size class j:

$$\mu_{\mathrm{pr}.j} = \sum_i \theta_{ij} \frac{j_{\mathrm{F}.i} B_i}{\epsilon_\mathrm{F} F_i}. \tag{3}$$

In addition to the predation mortality inflicted by larger plankton, the largest size classes are also exposed to predation by higher trophic levels that are not explicitly represented in the model, such as fish. The exposed size classes are those larger than m_{HTL} ($\mu\mathrm{g\ C}$), described by the selectivity function p_{HTL} :

$$p_{\mathrm{HTL},i} = \frac{1}{1 + (m_i/m_{\mathrm{HTL}})^{-2}}. \tag{4}$$

The higher trophic level mortality can either be a constant or proportional to the biomass concentration in the size class:

$$\mu_{\mathrm{HTL},i} = \begin{cases} \mu_{\mathrm{HTL},0}\, p_{\mathrm{HTL},i} & \text{constant} \\ \mu_{\mathrm{HTL},0}\, p_{\mathrm{HTL},i} \frac{B_i}{\ln(1/z_i)} & \text{``quadratic''} \end{cases} \tag{5}$$

where z_i is the ratio between the upper and lower sizes in the size class. It should be noted that higher trophic level mortality does not comply with the prey vulnerability due to motility that predation mortality follows. That is because higher trophic level organisms are expected to be visual predators and the hydrodynamic signals from prey motility do not affect the detection of prey. The inclusion of density-dependent regulation of predator mortality rates is essential for a realistic representation of top-down effects in simple food-chain models (Heath et al., 2014), therefore we use the density-dependent "quadratic" formulation in all simulations presented here, with $m_{\mathrm{HTL}} = 0.1\ \mu\mathrm{g\ C}$.

3.2 Cell model

The unicellular spectra can be either generalists or diatoms. The only differences between the two spectra are that diatoms have a vacuole, that they cannot perform phagotrophy, and that they have a lowered predation risk ($p < 1$) (as explained above). The present description of diatoms with a fixed vacuole size is a simplified version of the description with dynamic vacuoles in Hansen and Visser (2019); Cadier et al. (2020). The full set of equations and parameters for the unicellular model are given in Tables B1 and B2.

The cell model describes the encounter and uptake of resources and metabolism of an individual plankton cell as modulated by the cell's size (mass) m ($\mu\mathrm{g\ C}$). The size of the cell partly defines its trophic strategy, whether it is an osmo-heterotroph (a bacterium feeding mainly on DOC), a light- or nutrient-limited phototroph, or, for the generalists, a mixotroph (combining osmo-, photo-, and phagotrophy) or a heterotroph (living mainly on phagotrophy) (Andersen et al., 2016).

Regarding their morphology, we assume that cells are a spherical and consist of a cytoplasm surrounded by a membrane of thickness δ (Fig. 2). The diatom cells additionally have a vacuole that occupies a fraction v_{vac} of the cell volume and is surrounded by an additional inner membrane. The radius of a cell with mass m is approximately (assuming $\delta \ll r$) (eq. B5):

$$r = \left(\frac{3}{4\pi} \frac{m}{\rho} \frac{1}{1 - v_{\mathrm{vac}}} \right)^{1/3}, \tag{6}$$
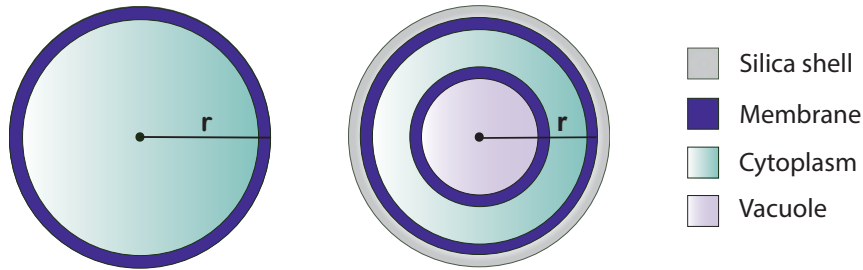
Figure 2. Geometry of generalist and diatom cells
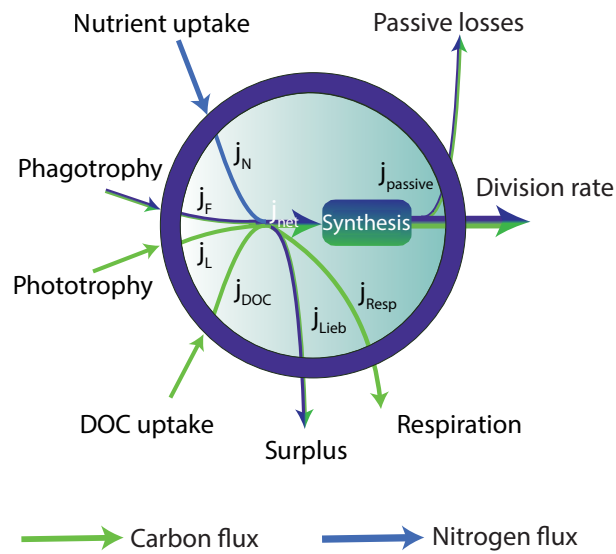
Figure 3. Illustration of the cell metabolism of a generalist with uptakes of resources as carbon (blue arrows) and nutrients (green arrows), losses due to respiration or passive losses, biosynthesis leading to cell division rate g, resulting in a net division rate. The diatom cell is similar, but with an additional uptake of silicate j_{Si} and no phagotrophic uptake.

where ρ is the density of the cytoplasm (μg C μm^{-3}). As part of the cell's mass is used for the membrane(s), the fraction of the cell mass available for active metabolism for diatoms is calculated in (eq. B6) and for generalists is (Andersen and Visser, 2023):

$$\nu = 3\frac{\delta}{r}. \tag{7}$$

The cell model describes three processes: encounter with resources, uptake of resources and metabolism, and mortality:

3.2.1 Encounter

185 The cell takes up carbon via photosynthesis (light), while both carbon and nitrogen are taken up via phagotrophy (i.e. eating prey; only generalists) and diffusion, in the form of dissolved organic carbon (DOC) and dissolved inorganic nutrients respectively (Fig. 3). Diatoms also take up silicate to build their silica shell. The encounter with the resources (light L, DOC, N, prey F, and silicate Si) is described as specific mass fluxes j_X (day^{-1}):

$$j_{\text{enc.X}} = a_X(m) X \rho_{C:X}, \text{ with } X \in \{\text{DOC}, \text{N}, \text{L}, \text{F}, \text{Si}\} \tag{8}$$

190 where $\rho_{C:X}$ is the ratio between carbon and the element of the resource X and a_X is the mass specific affinity.

The affinity for each resource uptake is determined by the geometric properties of the cell and is expressed as a function of mass (m) and the radius r. The dependency of affinities on size is analysed comprehensively in Andersen and Visser (2023) and given in Table B1. Generally, the diffusive uptake is limited by the cell radius, light uptake by the cell cross-sectional area, and feeding by the cell volume.

3.2.2 Metabolism

195

Uptake of resource X has a carbon cost $\beta_X j_X$. To avoid unnecessary respiration, the cell regulates the actual uptakes j_X from the encountered uptakes $j_{\text{enc.X}}$ to maximize cell division rate under the constraint of a fixed C:N:Si stoichiometry. The down-regulation of light intake acts as a simple representation of light-adaptation. The emergent respiration is:

$$j_{\text{resp}} = j_R + \sum_X \beta_X j_X + \beta_g g, \tag{9}$$

200 where j_R is the basal metabolism and $\beta_g g$ is the growth metabolism as a fraction of the division rate g. The cell division rate is limited by its capacity for biosynthesis j_{max}:

$$g = j_{\text{max}} \frac{j_{\text{net}}}{j_{\text{net}} + j_{\text{max}}} - j_{\text{passive}}, \tag{10}$$

where j_{max} is proportional to the active cell mass v (7), and j_{passive} are passive losses across the cell surface.

3.2.3 Population growth

205 Besides predation losses (eqs. 3 and 5) the cell is exposed to viral lysis with a mortality μ_2 proportional to the cell biomass:

$$\mu_{2.i} = \mu_2 B_i / \ln(\Delta m_i) \tag{11}$$

where Δm_i is the width of the size class (Fig. C1). The final growth equation for the unicellular plankton is:

$$\frac{dB_i}{dt} = (g_i - \mu_{\text{pr},i} - \mu_{\text{HTL},i} - \mu_{2,i}) B_i, \quad i \in \text{uni} \tag{12}$$

where uni = {all unicellular groups}.

3.3 Multicellular model

Copepods represent multicellular zooplankton and the copepod community consists of different populations. Each population is characterized by the adult body-mass and the feeding mode (active or passive). The spectrum for the population resolves the life stages of copepods, from nauplii to adults, following the description in Serra-Pompei et al. (2020):

$$\frac{\mathrm{d}B_i}{\mathrm{d}t} = J_{\mathrm{in},i} + (j_{\mathrm{out}.i} + g_i - \mu_{\mathrm{pr}.i} - \mu_0 - \mu_{\mathrm{HTL},i})B_i, \quad i \in \mathrm{multi} \tag{13}$$

where $\mathrm{multi} = \{\text{all multicellular groups}\}$.

Here J_{in} (μg C L^{-1} day^{-1}) is the mass flux into the size class, which equals the mass flux out of the previous class, except for the first class where it is the reproductive flux. g_i (day^{-1}) is the biomass accumulation rate and μ_0 (day^{-1}) is background mortality. The fluxes and the mortalities are calculated from the consumption by predation (eq. 2) and the predation mortality (eq. 3), and are detailed in Table B3.

3.4 Particulate organic matter (POM)

Particulate organic matter is produced by losses from plankton (Fig. 1). The POM has the same C:N ratio as the plankton, meaning that POM does not transport silicate; all lost silicate is remineralized directly into the dissolved fraction. POM is generated from several sources (Fig. 4): 1) a fraction $1 - \gamma_2$ of cells dying from lysis; 2) Multicellular plankton produce POM from sloppy feeding, fecal pellets (incomplete assimilation) and from the losses due to inefficient reproduction (egg mortality); 3) A fraction γ_{POM} of the losses from higher trophic level mortality is assumed to be fecal pellets routed to POM. Particulate organic matter is lost from remineralization with a rate r_{POM} and from grazing by copepods:

$$\begin{aligned}
\frac{\mathrm{d}B_i}{\mathrm{d}t} = \sum_j &\left[(1-\gamma_2)\mu_{2.j} + (1-\gamma_{\mathrm{F}})\frac{1-\epsilon_{\mathrm{F}}}{\epsilon_{\mathrm{F}}} j_{\mathrm{F}.j} + (1-\gamma_{\mathrm{HTL}})\mu_{\mathrm{HTL},j} \right] B_i \\
&+ \sum_{S \in \text{ multi adults}} (1-\epsilon_{\mathrm{R}})g_S B_S - (r_{\mathrm{POM}} + \mu_{\mathrm{pr}.i})B_i, \quad i \in \mathrm{POM},
\end{aligned} \tag{14}$$

where index S indicates the last (adult) size class in each copepod population. Parameters are given in Table B5.

3.5 Bio-geochemical dynamics

The dissolved state variables are taken up through diffusive encounter and replenish with the losses from the plankton groups (Fig. 4). The equations for the dissolved phases of nitrogen, DOC, and silicate are:

$$\frac{\mathrm{d}N}{\mathrm{d}t} = \left[\sum_{i \in \mathrm{uni}} (-j_{\mathrm{N},i} + j_{\mathrm{Nloss},i} + j_{\mathrm{passive},i} + \gamma_2\mu_{2,i})B_i + \gamma_{\mathrm{HTL}} \sum_{i \in \mathrm{multi}} B_i + r_{\mathrm{POM}} \sum_{i \in \mathrm{POM}} B_i \right] \frac{1}{\rho_{\mathrm{C:N}}} \tag{15}$$

$$\frac{\mathrm{d}C}{\mathrm{d}t} = \sum_{i \in \mathrm{uni}} (-j_{\mathrm{DOC},i} + j_{\mathrm{C.loss},i} + j_{\mathrm{passive},i} + \gamma_2\mu_{2,i})B_i \tag{16}$$

$$\frac{\mathrm{d}S}{\mathrm{d}t} = \left[\sum_{i \in \mathrm{diatoms}} (-j_{\mathrm{Si},i} + j_{\mathrm{passive},i} + \gamma_2\mu_{2,i})B_i \right] \frac{1}{\rho_{\mathrm{C:Si}}} \tag{17}$$
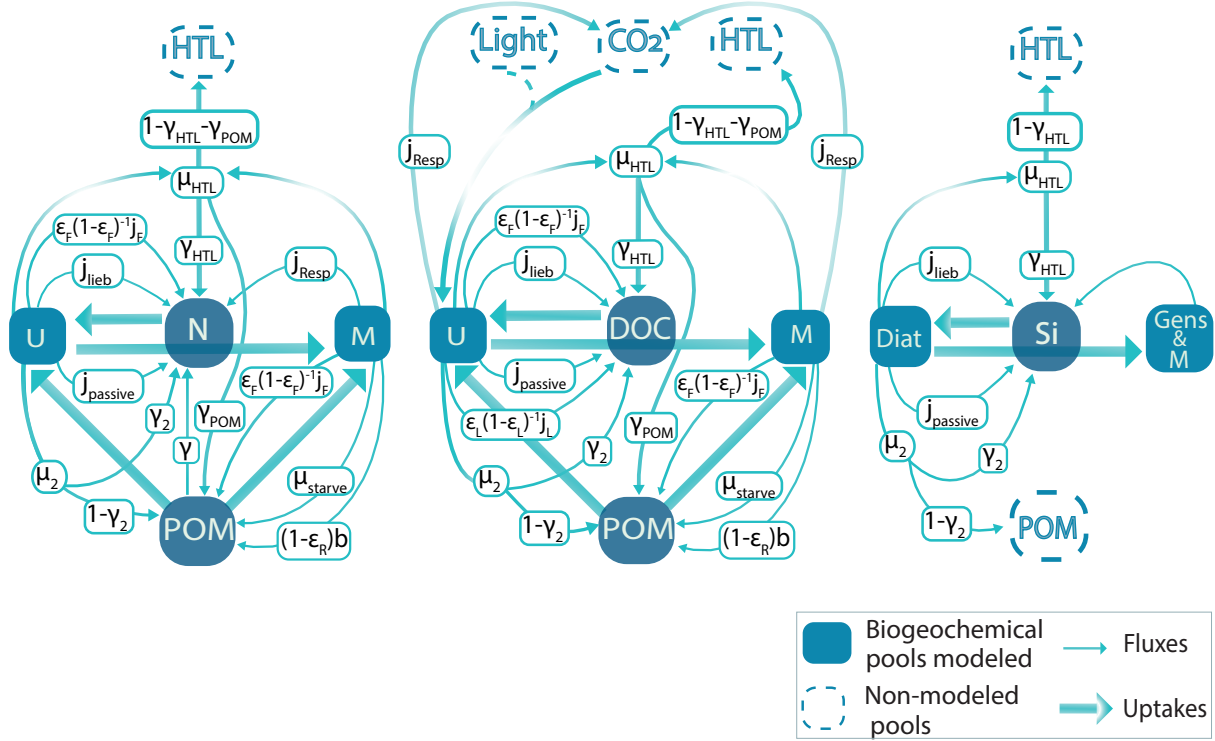
Figure 4. Representation of nitrogen, carbon and silica fluxes in unicellular (U) and multicellular (M) plankton. All rates are in units day^{-1}. In the chemostat setup POM sinks out to the deep (Eq. 20). The j's represent direct losses, the μ's represent mortalities, γ's represent fractioning of a flux into different pools (e.g. between direct remineralization and to POM), $b = J_{\text{in.1}}/m_{\text{egg}}$ is the copepod birth rate, and ε_{F} is feeding efficiency. Note that POM does not resolve silicate so all fluxes into POM are directly mineralized into dissolved silicate. Similarly for the silica fluxes, we assume that none of the silica in diatoms is assimilated by their predators and it all becomes remineralized.

3.6 Temperature

Temperature T (° C) influences the physical and the metabolic processes of all groups in the model. The influence of temperature is described via Q_{10} corrections to the parameters from a reference temperature of $10°$ as:

$$Q(T) = Q_{10}^{(T-10°)/10°}. \tag{18}$$

The only physical process influenced by temperature is the diffusion rate of dissolved matter (DOC and nitrogen) towards the cell, which has a $Q_{10} = 1.5$ (Serra-Pompei et al., 2019). This means that the parameter α_{N} is corrected by temperature (Table B2). The other temperature correction is on metabolic rates by $Q_{10} = 2$. The affected metabolic rates are: the basal metabolic rate (j_{R} for unicellulars and k_{R} for multicellulars), the maximum synthesis rates (α_{max} and h respectively), and the remineralization rate of POM r_{POM}.

3.7 Embedding within ocean physics

245 $$u_{t+1} = u_t + \kappa \frac{\Delta t}{\Delta z}(u_{\text{bottom}} - u_t), \tag{19}$$

where u is the state variable (N or S), t is the time step, Δt is the transport time step (0.5 day), Δz is the thickness of the bottom layer, $\kappa = 1/365 \, \text{m day}^{-1}$ is the relaxation rate, and u_{bottom} is the bottom concentration taken from World Ocean Atlas climatologies (Reagan et al., 2023).

The chemostat environment models the upper mixed layer which mixes with an unresolved deep layer, with a mixing rate d
250 (day^{-1}) (Evans and Parslow, 1985). The deep layer concentrations of nutrients are fixed, N_{deep} and S_{deep}, and thr concentration of DOC is zero. Unicellular organisms are mixed out of the upper layer, while the multicellular organisms are assumed to stay in the upper layer. POM is mixed out of the surface layer but also sinks out with a rate v/M, where v (m day^{-1}) is the sinking velocity and M (m) the thickness of the mixed layer. The governing equations are solved with the internal matlab Rosenbrock 2nd order stiff solver:

255 $$\frac{\mathrm{d}B_i}{\mathrm{d}t} = f_i(L,T,\mathbf{B}) + \underbrace{d(B_{\text{deep}.i} - B_i)}_{\text{for nutrients and uni.}} - \underbrace{\frac{v}{M}B_i}_{\text{for POM}} , \tag{20}$$

where the first term $f_i(L,T,\mathbf{B})$ is the right-hand-side of the state-variable equations (12-14), which depends on light L, temperature T and the set of all the state variables $\mathbf{B}$. Finally, the chemostat can be run in a seasonal environment where light, temperature, and mixing rate d vary with time and are extracted from the transport matrix. In high latitude environments it is necessary to disable the mixing of unicellular plankton to the deep layer to allow them to survive the winter period.

260 3.8 Model setup and numerical solution

The model framework allows for a flexible combination of the four groups. A model setup requires at least one unicellular group (generalists or diatoms), and may include POM and a number of copepod groups, however the default NUM model setup used here involves all four groups. Each group contains a number of size classes and the model results depend, to some degree, on the number of size classes used in the unicellular groups (Fig. 5a,b) and in the copepod groups (panels c,d). Further,
265 it depends on the number of active-copepod and passive-copepod groups (panels e,f). The number of size classes and copepod groups in the default NUM model setup is chosen such that the overall results, in terms of size spectra (Fig. 5a,c,d) and ecosystem function (panel b,d,f), do not change considerably upon the addition of more classes or groups. The setup includes 10 size classes of generalists, 10 size classes of diatoms, two passive copepod groups (adult sizes 0.2 and 5 μg C), and three active copepod groups (1, 32, and 1000 μg C), where each group is discretized in 6 size-classes representing the growth in
270 body mass. The number of state variables adds up to a total of 54.

Running the NUM model from the matlab interface proceeds in three steps: 1) setting up the simulation type (i.e., choosing which size spectra groups to simulate), 2) setting up the simulation environment (chemostat, water column, or global), and 3) running the model:

```
p = setupNUMmodel( bParallel=true ); % Model setup
```
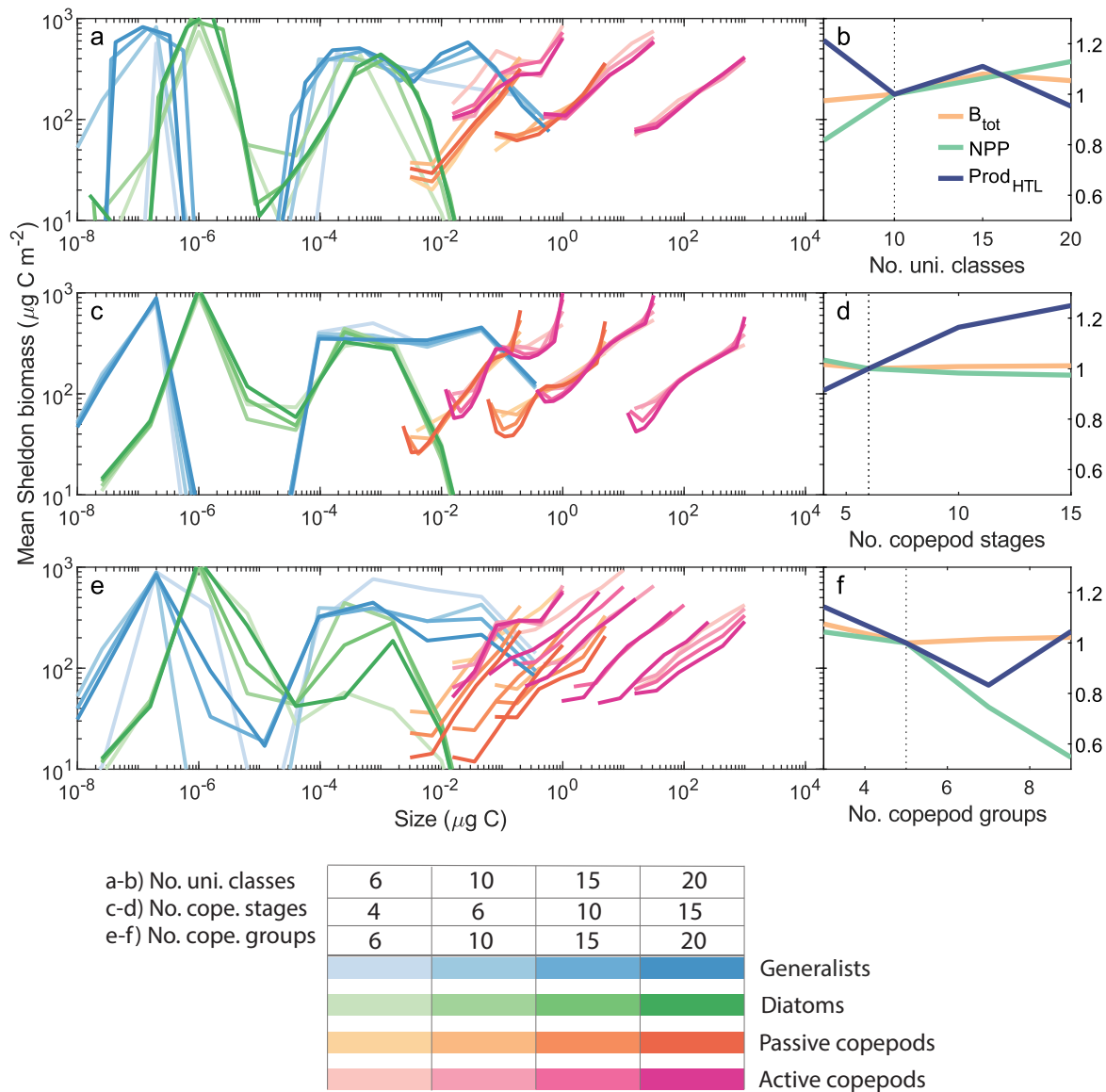
Figure 5. Sensitivity of the model to number of unicellular size classes (a-b), number of copepod stages (c-d), and number of copepod groups (e-f). The left column of panels show the Sheldon size distributions (Andersen and Visser, 2023, Box V) and the right column shows total biomass (orange), NPP (green), and HTL production (dark blue) normalized by the value in the standard setup (vertical dashed line). All runs are from a simulation of the water column model at 60°N and 15°W. Color intensity indicates number of classes/groups. In the left panels, blue shades represent generalists, green diatoms, orange-red passive copepods and magenta active copepods.

```
275  p = parametersGlobal( p );          % Model environment
     sim = simulateGlobal( p );          % Run simulation
     plotSimulation( sim );
```

All parameters are encapsulated in the `p` structure, which is passed to the simulation (in this example a global simulation). The simulation returns the entire output in the `sim` structure which is passed on to other functions for analysis or plotting. These

280 two structures are documented on the github site and all functions are documented in their `help` pages.

3.9 Calibration and evaluation data

All parameters of the plankton groups are based on first principles or cross-species comparisons (Andersen and Visser, 2023; Serra-Pompei et al., 2020). While these parameters are uncertain (explored byHansen et al. (2024)), they are not expected to vary spatially. However, some of the extrinsic parameters either have no first-principle arguments or data, and/or are varying

285 spatially. These extrinsic parameters together mold the overall function of the community: the global average light extinction coefficient by water k_w without feedback from plankton, the average POM sinking velocity v, and the higher trophic level mortality $\mu_{\mathrm{HTL.0}}$. These variables conjointly determine the total biomass and production of the global model: lower light extinction increases gross primary production, lower sinking velocity decreases the remineralisation depth and thereby increases the amount of primary production. Lower higher trophic level mortality increases the copepod biomass, which influences the

290 unicellular spectrum through a trophic cascade (Fig. F5). In nature, the values of these three variables vary on a global scale, but here they are kept constant. Consequently, we must calibrate to find reasonable global average values. We calibrate by minimizing the error between average modeled and observed values of net primary production (NPP), picoplankton, particulate organic carbon, and copepods. The minimized bias is:

$$\varepsilon = \frac{1}{6}\left[\sum_{i=1}^{3}\frac{1}{n_i}\sum_{j}^{n_i} \log\left(\frac{Q_{\mathrm{model.}ij}}{Q_{\mathrm{obs.}ij}}\right) + \sum_{i=1}^{3}\log\left(\frac{P_{\mathrm{NPPmodel.}i}}{P_{\mathrm{NPPobs.}i}}\right) \right] \tag{21}$$

295 where the first addend is the mean error between n_i observations of picoplankton ($i = 1$), POC ($i = 2$), and copepods ($i = 3$), and the second addend is NPP measurements taken at three sites that represent markedly different environments.

We use four data-sets for calibration: 1) Picophytoplankton biomass (organisms with a diameter less than 2 μm) between 0 and 10 m depth from water samples between 1997 and 2014, across all latitudes mainly in the Atlantic Ocean (fig. E3) (Martínez-Vicente et al., 2017); 2) Particulate Organic Carbon (POC) biomass of all plankton and detritus particles with a

300 radius between $0.35 - 15$ μm from the GO-POPCORNv2 dataset (Tanioka et al., 2022) from cruises (2011-2020) across all major ocean basins, spanning from 70°S to 55°N (fig. E2); 3) Copepod biomasses across the Atlantic Meridional Transect cruises (López and Anadón, 2008); 4) NPP annual averages (2002-2021) from satellite observations processed with the CAFE model, selected it due to its better performance on a global average relative to other satellite-derived NPP models (Silsbe et al., 2016). The three sites chosen for comparison are: an oligotrophic location (22°N, 158°E), a eutrophic location (5°N, 119°W),

305 and a seasonal location (60°N, 15°W). At these sites, the annual averaged NPP over the entire water column from CAFE is approximately 200, 1000, and 500 mg C yr^{-1}, respectively.

Net primary production is calculated in the model as the amount of carbon that is fixed by photosynthesis minus what is used for respiration:

$$P_{\text{NPP}} = \sum_{i \in \text{uni}} \max\{0, (j_{\text{L}.i} - j_{\text{resp}.i})B_i\}. \tag{22}$$

310   This definition seems innocuous enough but there are two important comments. First, all mixotrophic metabolic costs are included in the respiration (j_{resp}) that is subtracted from the fixed carbon (j_{L}), including the costs of feeding and DOC uptake. This is different from the usual thinking about primary production, which implicitly assumes that primary production only occurs by obligate phototrophs. The assumption made here is that fixed carbon is prioritized for respiration over carbon acquired from DOC and feeding. Second, it should be noted that the definition here does not include all primary production. Some carbon

315   is lost to DOC during the uptake process (Fig. 4b), which can fuel osmotrophic biomass production. Adding this potential carbon production into the definition can be achieved by replacing j_{L} with $j_{\text{L}}/\epsilon_{\text{L}}$. However, we refrain from that, because the measures of NPP that we compare with are based on the pure phototrophic biomass production.

After the initial calibration of the three parameters we evaluate the performance of the NUM model using a second set of observations. For the performance evaluation we use observations of nano- and microplankton from three Atlantic Meridional

320   Transects cruises (Rodríguez-Ramos et al., 2015), a meta-analysis of global mesozooplankton biomass distribution (Moriarty et al., 2013), and annual averages of surface nutrients from the World Ocean Atlas (Reagan et al., 2023).

4   Results

Simulations are initiated with concentrations of inorganic nitrogen and silicate from the World Ocean Atlas (Reagan et al., 2023). Biomass distributions equilibrate quickly and after 10 years are well converged (Fig. F6b, d). Deep nutrient concen-

325   trations are on a long slow transient, particularly away from seasonal environments (Fig. F6a, c), with a weak effect on the biomass distributions. The simulations presented in the following are after 10 years of simulation.

We first show the model calibration followed by the model global biomass distributions. We then assess performance with evaluation data, show how the three model environments (global, water column, and chemostat) compare, and finally show outputs related to the physiological dynamics of the organisms in the model. The results are produced from 10-year simulations

330   with the standard NUM model setup (3.8).

4.1   Model calibration

The calibration gave an optimal light extinction coefficient of 0.07 m^{-1}, a sinking velocity of 13 m day^{-1}, and a coefficient of higher trophic level mortality of 0.005 L/(μg C day). The calibrated model produces biomasses of picoplankton, POC, and copepods which are in the correct order of magnitude of the observations (Fig. 6a-c). Though the model is only calibrated to

335   the average values, it does produce latitudinal patterns in accordance with the observed patterns (Fig. 6d-f: elevated biomass at temperate latitudes (-50° and 50°) and to a smaller degree around Equatorial upwelling. The modeled copepod biomass approximates observations at temperate latitudes, however, it underestimates copepod biomass in the Equator.
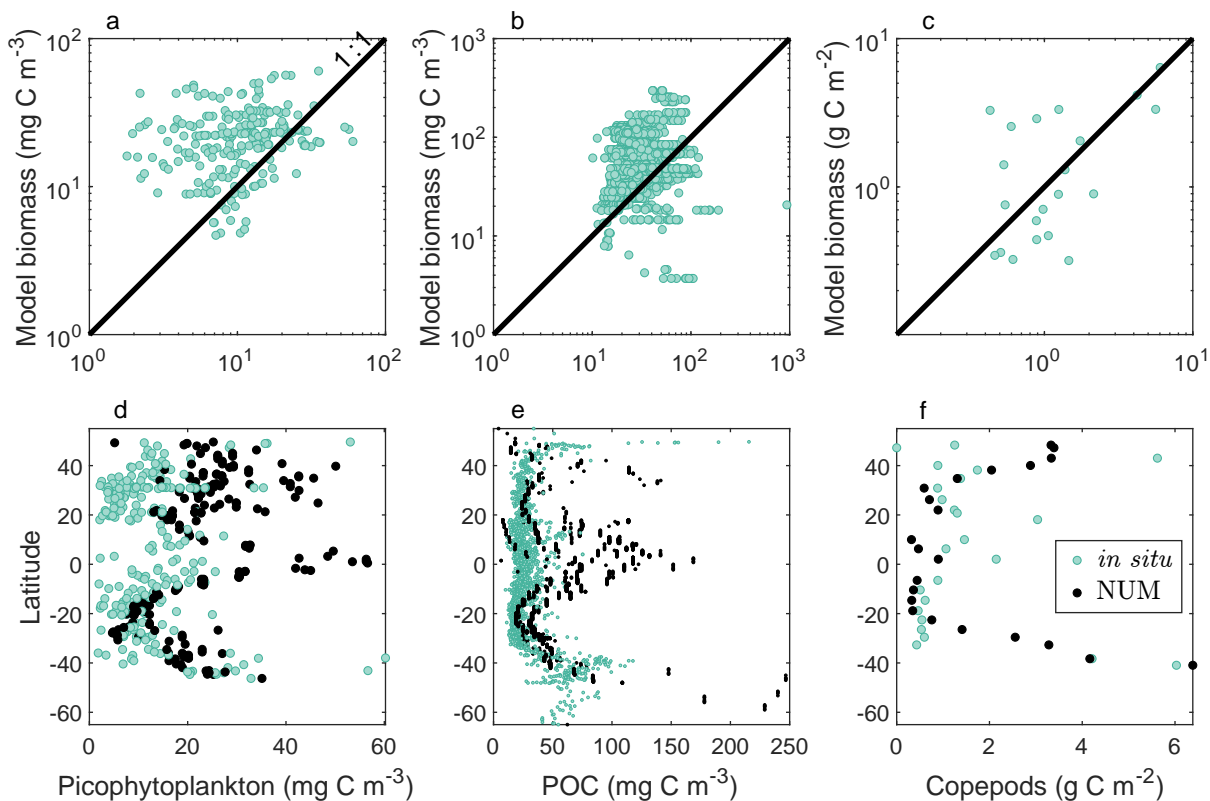
Figure 6. Comparison of model biomass output to *in situ* calibration data for biomasses of picophytoplankton (a, d), particulate organic carbon (b, e), and copepods (c, f). The top row shows modelled biomasses on the y-axis and observations on the x-axis. The bottom panels show the latitudinal variation of biomasses. Mean biases are 0.687 (a), 0.653, (b), and 0.016 (c), calculated from eq. 21.

4.2 Modeled biomass and productivity

The model captures general global-scale biomass patterns, with higher concentrations of unicellular and multicellular plankton
340 in high-latitude seasonal environments and equatorial upwelling areas and the lowest biomasses in oligotrophic gyres (Fig. 7). These patterns are mirrored in satellite-derived NPP estimates (Fig. 8). The figure highlights the big variation in the satellite observation products. One unrealistic pattern is the very high biomass and production in the Southern Ocean.

4.3 Model evaluation

Turning to the evaluation data from the Atlantic transects, we see that the model captures the right order of magnitude of nano-
345 and micro-plankton biomasses (Fig. 9). In these data, the equatorial upwelling is less pronounced which is also reproduced by the model . However, the model overestimates plankton biomass at higher latitudes compared to the AMT 14 cruise (Fig. 9d), where samples were collected during May.
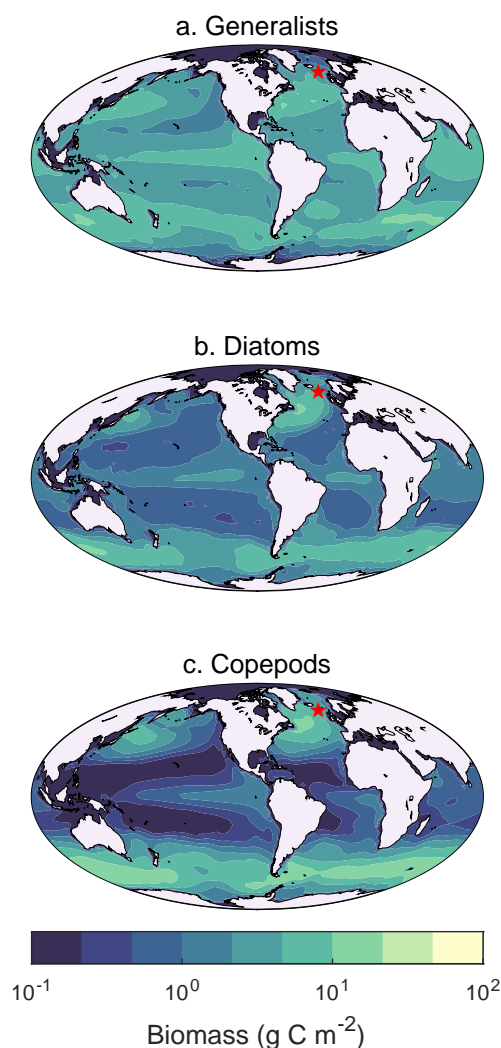
Figure 7. Global annual average biomass of (a) generalists, (b) diatoms and (c) copepods. The red star indicates the location (60°N,15°W) that is used for evaluate the seasonal dynamics in later figures.

On a global scale it appears that the average mesozooplankton (copepod) concentration is somewhat higher in the model than observed (Fig. 10).

350   The model resolves nitrogen in a simplified manner without accounting for its different forms (i.e. nitrate, nitrite, ammonia). We have chosen nitrate for the comparisons because it is considered to be the main nitrogenous compound utilized for primary production (Lenton and Watson, 2000). The model captures the spatial patterns in annual mean nitrogen concentration at the surface (Fig. 11 a, b) with high values in the North Atlantic and Southern Ocean and lower at the oligotrophic gyres. In addition, it reproduces elevated concentration in upwelling areas and in the Indian Ocean. Looking at the order of magnitude of nitrogen concentrations, NUM is more accurate in the North Atlantic, Southern Ocean and oligotrophic areas, while for the rest of
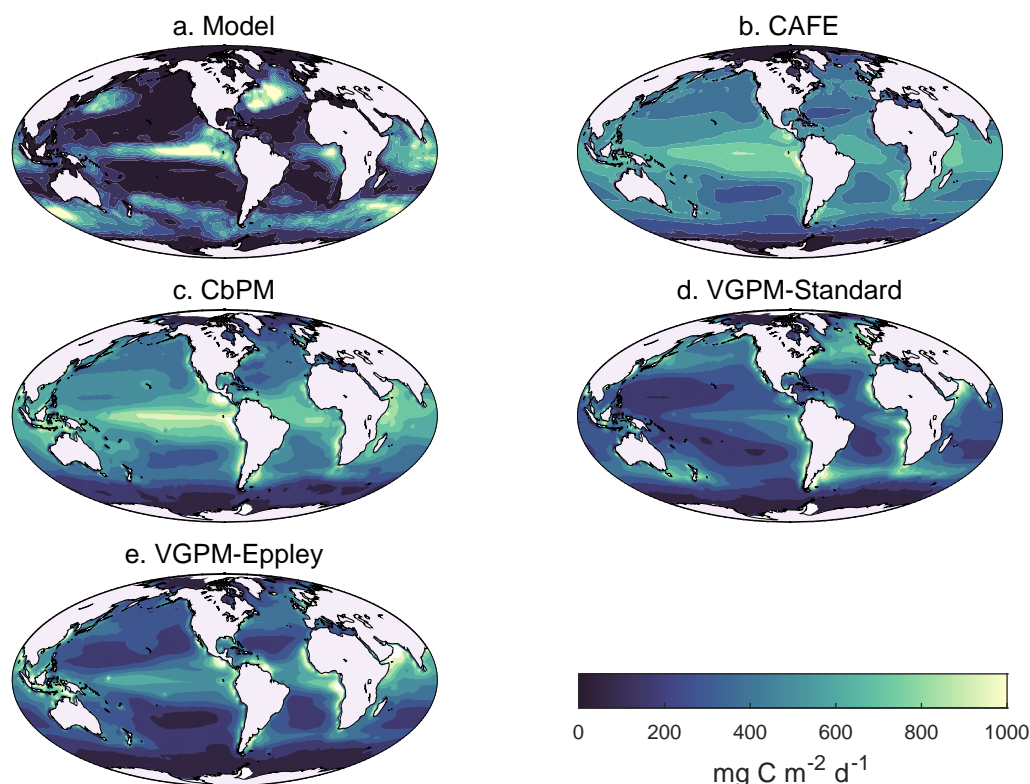
Figure 8. (a) NUM annual mean NPP,(b) CAFE estimated annual mean NPP (Silsbe et al., 2016), (c) CbPM estimated annual mean NPP (Westberry et al., 2008), (d) VGPM-Standard estimated annual mean NPP (Behrenfeld and Falkowski, 1997), and (e) VGPM-Eppley estimated annual mean NPP (Behrenfeld and Falkowski, 1997), all datasets from (Ocean Productivity). Units are mg C m^{-2} d^{-1}.

the global ocean it underestimates these values. Silicate patterns are only captured at high latitudes and to a lower degree in the Equatorial Pacific. For the rest of the ocean the values are very low, which explains why larger diatoms only proliferate in the North Atlantic and Southern Ocean in our simulations (Fig. 11 c, d). Lack of external nutrient sources, such as from atmospheric deposition and rivers could explain the underestimated values. Thus, the concentrations rely on remineralization of POM and Si, while the initial concentration from World Ocean Atlas are transported to the bottom, e.g. in the oligotrophic gyres. Another reason behind low nutrient concentrations could be that unicellular plankton in the model are very effective in taking up nutrients.

4.4 Model simulations

The unicellular NUM model's output differs from traditional biogeochemical plankton models: instead of having state variables of bacteria, phytoplankton, and zooplankton, the NUM model resolves generalists and diatoms. While the diatoms are obligate phytoplankton, the trophic strategies of the generalists are dynamic and an emerging property of the model. However, common terminology and most models explicitly resolve state variables of bacteria, phytoplankton, and zooplankton. To
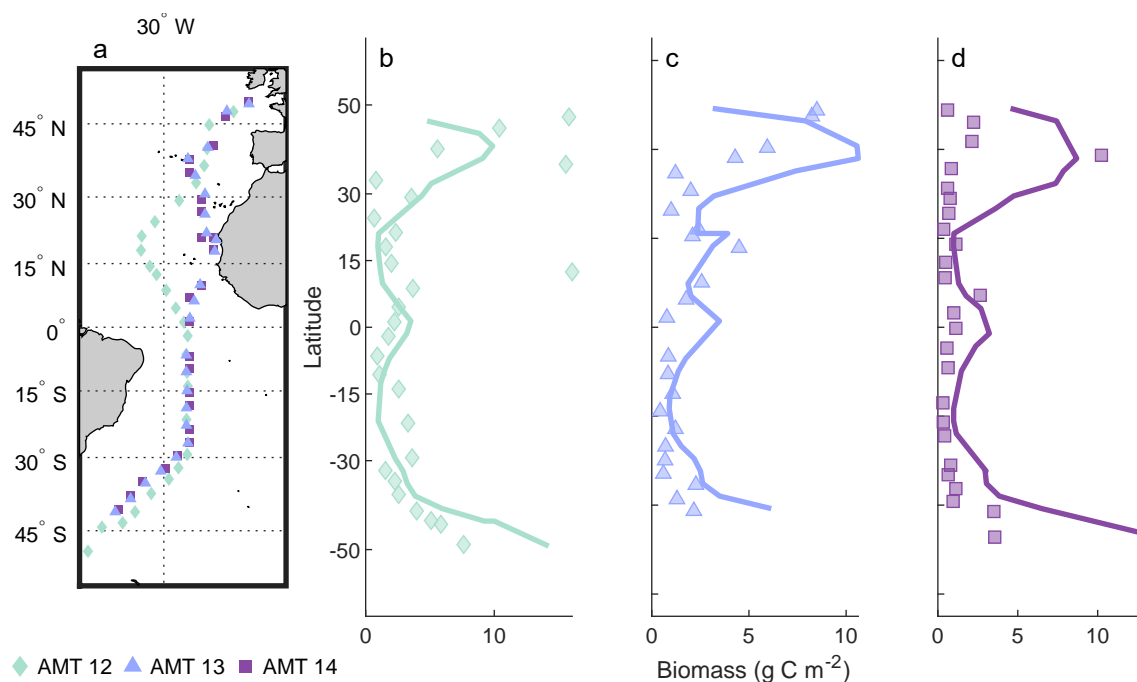
Figure 9. Biomass of nano- (2-20 μm radius) and micro-plankton (20-200 μm radius) of the model (line) compared to AMT data (markers). a: Transects of the different AMT cruises, b: AMT 12: May-June, c: AMT 13: September-October, d: AMT 14: May. The modeled biomass is the depth-inegrated average of the respective months for each cruise, extracted from the final year of a 10-year global simulation.
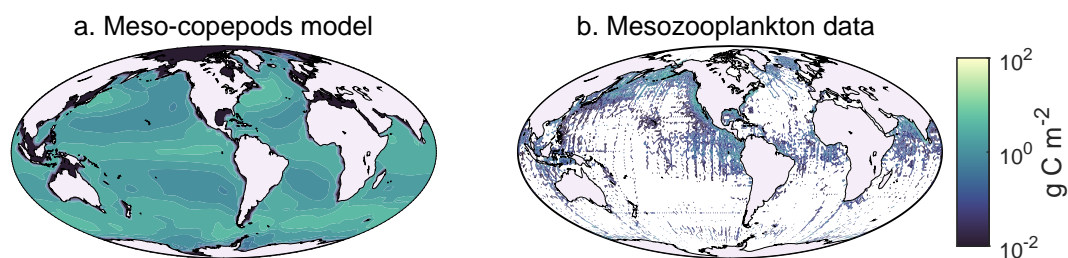
Figure 10. Annual mean mesozooplankton biomass. Observation data from (Moriarty et al., 2013) (integrated over the top 150 m) compared to model output (top 170 m).

relate the model's output to the aforementioned groups, we can estimate bacteria, phytoplankton, and zooplankton biomass from the generalists and diatoms, by weighing each size class with the fraction of carbon assimilation from DOC (bacteria),
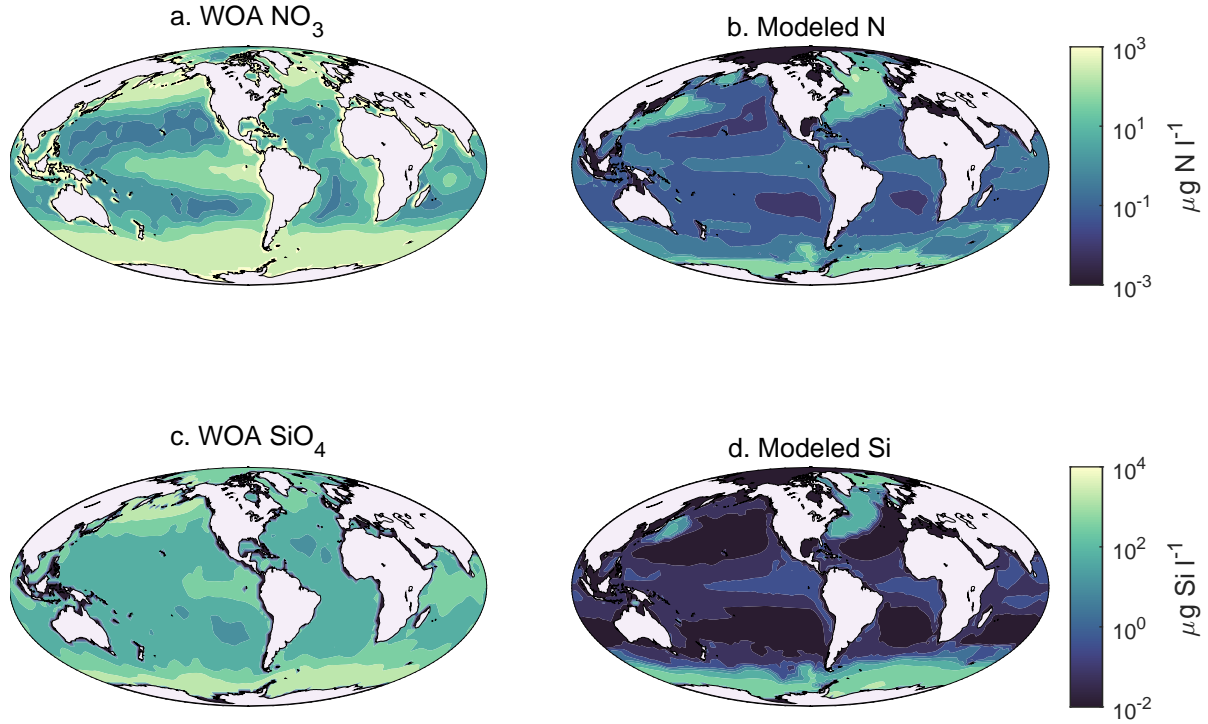
Figure 11. Annual mean concentrations of (a-b) nitrate (μg N l^{-1}) and (c-d) silicate (μg Si l^{-1}) in the top 5 m. World Ocean Atlas (WOA) observations (left) compared to model output (right).
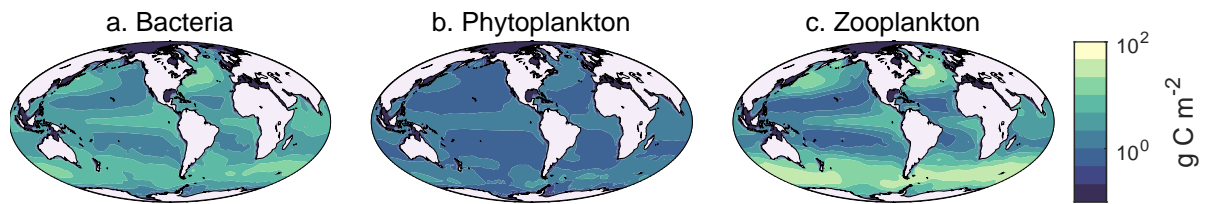
Figure 12. Annual depth-integrated mean biomass in the model: (a) bacteria biomass, (b) phytoplankton, (c) zooplankton, including unicellular plankton (mixotrophs and phagotrophs) and copepods, all calculated from Eqs. 23-25.

370   photosynthesis (phytoplankton), and phagotrophy (mixotrophs/zooplankton):

$$B_{\text{bact}} = \sum_i \frac{j_{\text{DOC}}}{j_{\text{C}}} B_i \tag{23}$$

$$B_{\text{phyto}} = \sum_i \frac{j_{\text{L}}}{j_{\text{C}}} B_i \tag{24}$$

$$B_{\text{zoo}} = \sum_i \frac{j_{\text{F}}}{j_{\text{C}}} B_i, \tag{25}$$

where $j_{\text{C}} = j_{\text{DOC}} + j_{\text{L}} + j_{\text{F}}$ (Fig. 12a-c).
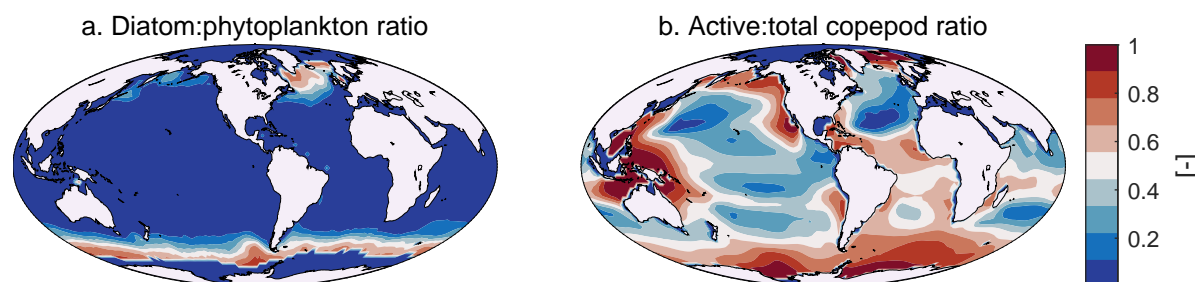
Figure 13. (a) Ratio of phototrophic diatom biomass to total phytoplankton biomass, and (b) ratio of active-feeding copepods to total copepod biomass.

Figure 13(a) shows the ratio of phototrophic biomass to the phototrophic part of the diatoms (diatoms can also take up dissolved DOC and therefore a fraction of their biomass will be categorized as bacteria). This result implies that the majority of phototrophs at high latitudes is diatoms, driven by the high influx of silicate during winter. This concurs with observations in the Pacific (Endo et al., 2018) and the Atlantic Oceans (Marañón et al., 2000).

The copepod community is dominated by active copepods in higher latitudes (Fig. 13b) and by passive (ambushing) copepods in oligotrophic gyres. In equatorial regions the presence of active copepods varies in different oceans. In the Equatorial Atlantic active copepods occupy between 50 and 60% of the multicellular plankton community, where there are abundant food resources to support their growth. In the Equatorial Pacific though, passive copepods dominate, possibly because there small primary producers are more common (Chavez et al., 1996; Mackey et al., 2002), whose size is preferred by these copepods. Lastly, active copepods occupy 60 to 80% of copepods along boundary currents in the Pacific, namely the California Current east and Kuroshio Current west, both known to be highly productive systems (Kudela et al., 2008; Lee Chen et al., 2008) that can support larger predators.

4.5 Comparison of environment setups

We compared runs of the water-column and seasonal chemostat model setups to the output from a global simulation at a high latitude location (Fig. 14) that is seasonally stratified. We chose a seasonally stratified location because it exhibits the succession of oligotrophic and eutrophic conditions throughout the year. The seasonal dynamics of total biomass show similar dynamics in the global an water-column simulations (panels a and c): a bloom in spring throughout the water column, followed by a deeper production maximum in summer, and terminated by a smaller autumn bloom. The spring bloom of diatoms is terminated first by silicate limitation, and the generalist bloom follows a bit later by nutrient limitation (Fig. F3 b,a). Contributing to the demise of the bloom is the grazing by copepods, which become established over summer (panels f-h). The deep maximum is less well represented in the global simulation, with only 13 vertical levels, than the water column simulation with 21 levels.

The size spectra show an overall similar community structure for the global ocean, water column and chemostat simulations (Fig. 14b,d,e). Diatoms deviate notably among the simulations: in the chemostat (Fig. 14e) with large diatoms dominating in the chemostat simulations while being outcompeted by generalists in the global water-column simulations. The preeminence
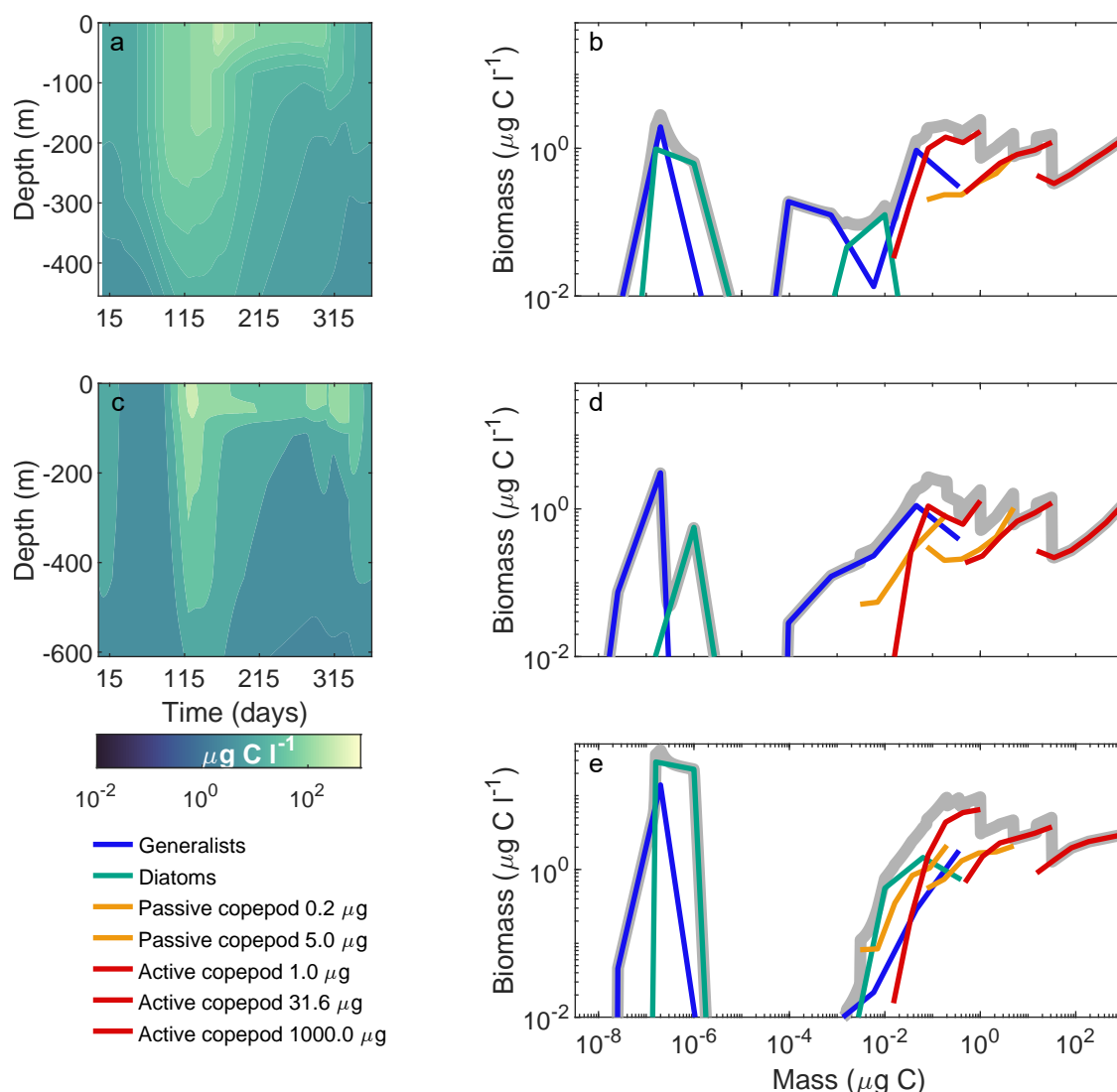
Figure 14. Model output for a 10-year simulation in the global, water column, and chemostat environments at a seasonally stratified location (60°N, 15°W) (red star in Fig. 7). (a) Total biomass in a water column extracted from the global simulation. (c) Total biomass in the same water column, but extracted from the water-column simulation. (b),(d),(e): Sheldon spectrum of the community from global, water-column, and chemostat simulations at 5 meters depth and averaged over the last year.

of large diatoms in the chemostat may result from the differences in mixing between the global and water-column simulations

400   versus the chemostat simulations. The global and water-column mixing will lead to a loss of the organisms to the deep water, where they will die unless they are mixed back up into the photic zone. In the seasonal water-column this mixing does not occur, as the organisms are expected to stay in the upper layer. As the mixing losses are most severe for the larger phytoplankton (like diatoms), with a low rate of photosynthesis, the absence of mixing losses in the chemostat gives them an advantage in the
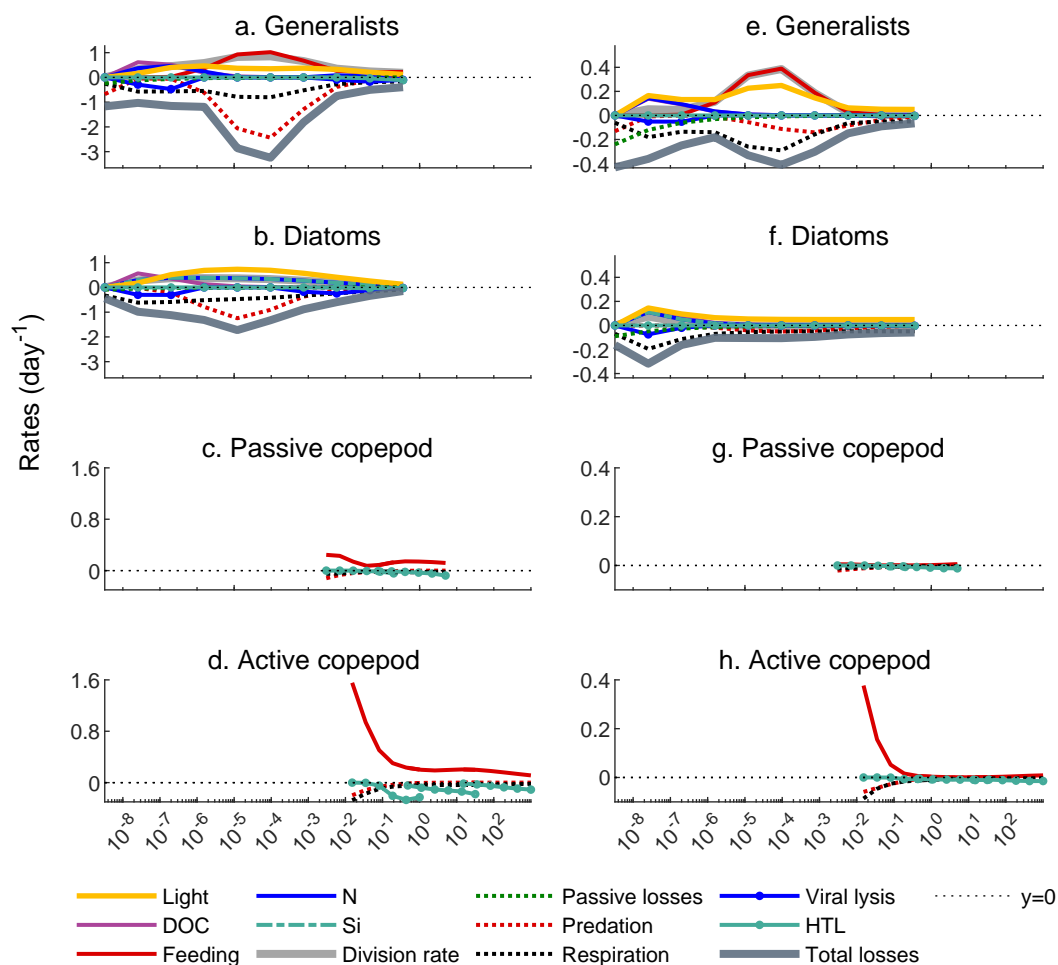
Figure 15. Gains and losses as a function of cell/body size in the spring bloom (April, left) and the summer (July, right). The lines above the horizontal dashed line shows gains either of carbon (from DOC uptake or photoharvesting; magenta and yellow), nutrients, silicate (blue and green), or a combination of carbon and nutrients from predation (red). The lines below the dashed lines shows losses of carbon from respiration (dashed black) or mortalities from predation (dashed red) or viral lysis (blue). The division rate is shown with thick grey. The output is from the chemostat simulation in Fig. 14d. Note the differences in the y-axes ranges between the left and right columns.

chemostat, and therefore contribute to their dominance. This behavior of the model should be kept in mind upon assessing the

405 global distribution of generalists and diatoms. Nevertheless, the output of the water column illustrates the same dynamics as the global at the same site, indicating that the water column model – which is naturally much faster than a global simulation – performs well. It should be noted, though, that the water column simulations perform best in seasonal environments. In less seasonal environments, the absence of advection appears to result in too low production (Figs. F1,F2).
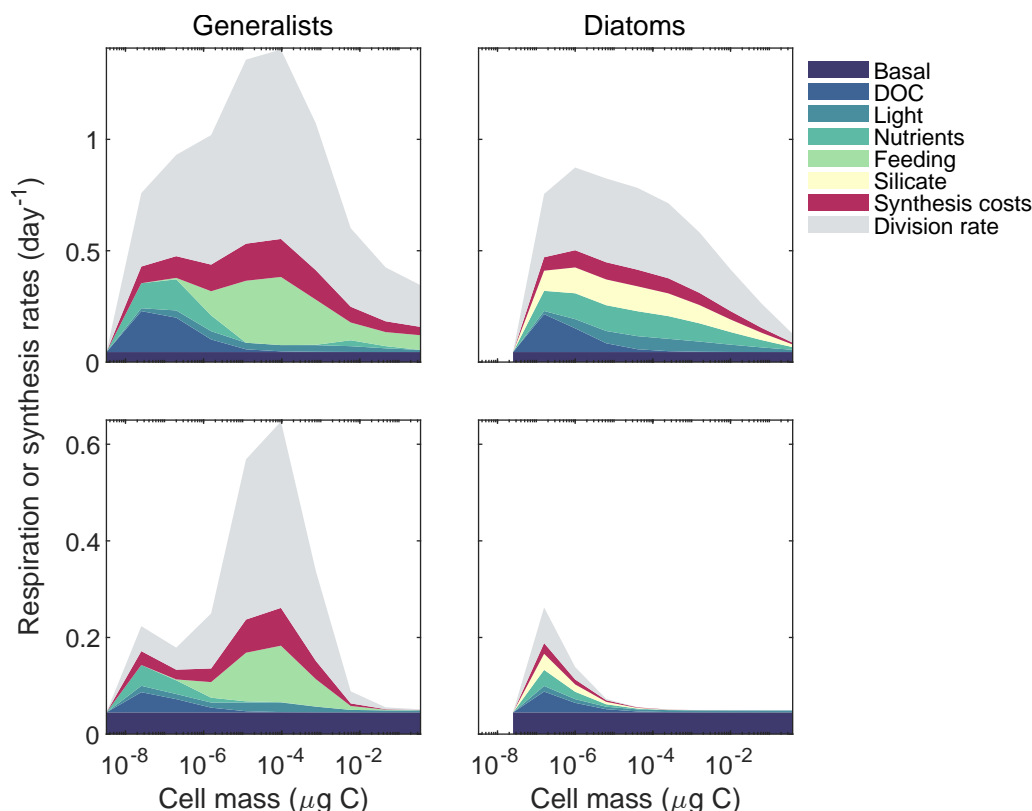
Figure 16. Metabolic budgets for generalists (left) and diatoms (right) in April (top panels) and July (bottom panels) extracted from Fig. 15. The division rate represents the uptakes that are used for synthesis of new biomass.

4.6 Individual-level processes

410 The NUM library makes it possible to extract descriptions of the rates that drive the dynamics of each size class. Fig. 15 shows the rates of the generalists, diatoms, and copepods from the chemostat simulation in Fig. 14d, with uptakes of resources (or prey) illustrated as positive rates and losses including mortalities as negative rates. Overall, the rates of uptakes and losses are much higher in the spring bloom (left column) than in the summer (right column). The spring panels portray strong predation pressure on the unicellular community (dashed red lines in panels a and b), indicating that the bloom is decaying at this time.

415 The high predation is also reflected in high feeding rates of the copepod community (red lines in panel c and d). Therefore, the spring copepod community is acquiring biomass at the expense of the unicellular community. In contrast, during summer, the division and loss rates in the unicellular community are roughly equal (grey lines in and panel e and f). This indicates a community in balance with little changes in biomass. Further, in the unicellular community, the figure shows how the trophic strategies change with cell size (Andersen et al., 2016): for the smallest cells, the acquisition of carbon is governed by DOC

420 uptake (magenta lines), and dissolved nutrients (blue lines), in particular in the spring bloom (panels a and b). Larger sizes

of generalists combine phototrophy (yellow lines) for carbon uptake with predation (red lines) for nitrogen. Larger sizes of diatoms are purely phototrophic (negligible uptake of DOC) and are limited by nitrogen and silicate uptakes during summer.

The regulation of uptakes by unicellular plankton (section 3.2.2) entails that the respiration budget is resolved explicitly among the carbon used for synthesizing new biomass and different respiratory costs of basal metabolism, uptakes of dissolved 425 nutrients and carbon, specific dynamic action of feeding (digestion), and costs of synthesizing new biomass (Fig. 16). In general, the synthesis of new biomass (the division rate) is one third of the total metabolic budget (Fenchel, 2013), while the respiratory costs are distributed among the different uptake costs, and a small portion is allocated to basal metabolism.

5 Discussion

We have presented a computational library for ecological modelling of plankton communities that resolves their utilization of 430 resources, their trophic strategies, their size-structured population dynamics, and their production of dissolved and particulate organic carbon. The library includes a high-level interface to simulate the communities on global scale, in a water column, or in a chemostat. Because the model includes copepods, which are often weakly represented in biogeochemical models, the model lends itself to linking with fish production models, or to modelling the carbon pump arising from copepod fecal pellets and plankton carcasses. Overall the NUM model is an intermediate-complexity model laboratory for ecological simulations 435 that is accessible to marine ecologists without biogeochemical or physical oceanography background. The focus here has been on the presentation of the general and flexible programming library and the calibration of the core NUM model setup.

The library has been designed with flexibility in mind. It can be run fully from a high-level programming language (mainly matlab). As the core library is written in Fortran, it is straight-forward to implement the model in a full circulation model (Hansen et al., 2024), for example using the FABM interface (Bruggeman and Bolding, 2014). Further, new size-spectrum 440 groups are easily written and added to the library. While POM described here is a single-state variable, the model does include a module to handle POM as an entire size spectrum. A more complex POM module is currently underway (Visser et al., 2024). Future extensions would be the inclusion of an iron nutrient tracer to limit the production in the Southern Ocean, a diazotroph spectrum to include nitrogen fixation, and a description of calcifiers.

Another flexible aspect of the NUM library is the possibility of performing simulations in three environmental settings: 445 global, water column, and chemostat. Water-column or chemostat simulations are useful for making fast model development or trial simulations before moving to full global simulations. However, it should be noted that, even though the three settings are based on the same transport matrix, there are differences in the output between them. First, the seasonal variation of total biomass both in the global and water column simulations at a high-latitude location concur: a spring bloom throughout the water column, followed by a deeper production maximum in summer, and a moderate short autumn bloom. However, the 450 global simulation reproduces the deep maximum less accurately than the water column one, due to a lower vertical resolution. While the structure of the water-column simulations corresponds relatively well with the global simulations in a strongly seasonal environment, they do not match well outside high-latitude environments, probably due to the absence of advective processes in the water-column simulation. Further, we observe disparity in the size spectra of the community extracted from

global, water column, and chemostat models. In particular, the dominance of large diatoms in chemostat simulations, emerges

455 from the absence of mixing losses of plankton in the seasonal chemostat simulations. This finding points to the importance of a better understanding of plankton's ability to maintain a position in the photic zone despite vertical mixing.

Diatoms have been included here as a new size spectrum group. The module is based on an extension of the generalist module with the addition of a vacuole and a silicate shell. In this manner, the diatom module does not use any diatom-specific parameters, apart from the cost of silicate uptake and the size of the vacuole, but is based on exactly the same parameters as the

460 generalists. In light of this very simple description of diatoms, the module performs quite well, as it captures the emergence of large diatoms during spring blooms in seasonal environments and their dominance in high latitudes (figs. 7b,13a). Nevertheless, it can be improved in mainly two areas. First, the diatoms act as both phototrophs and osmoheterotrophs (they take up dissolved DOC). The smallest diatoms are predominantly osmoheterotrophs (bacteria) and they often outcompete generalists. This may occur because the lower size limit for diatoms in the model is rather small, whereas diatoms smaller than 10^{-6} μg C are rarely

465 observed (Brzezinski, 1985; Pančić et al., 2019). Including this effect would make the smaller diatoms competitively inferior to the smaller generalists. Further, while larger phototrophic diatoms appear in high latitude seasonal regions, they are missing in upwelling regions in the global and water-column simulations (though they do appear in chemostat simulations). The absence of phototrophic diatoms in upwelling regions simulated in the model is implausible, given their known prevalence in such nutrient-rich waters (Benoiston et al., 2017). We conjecture that the absence of large diatoms is due to mixing losses. In the

470 chemostat simulations mixing losses of unicellular plankton are ignored, while plankton are mixed vertically in the global and water column simulations by the transport matrix. A future fix could be to include buoyancy control in the diatom module to avoid mixing diatoms out and thereby limiting their mortality.

All processes in each size-spectrum group are parameterized from considerations from first principles or from cross-species analysis of laboratory observations. The only calibrated parameters are those that form the closure of the model with respect to

475 light absorption (light absorption coefficient), nutrient turn-over rate (sinking speed of POM), and mortality on higher trophic levels. Each of these parameters are expected to vary significantly across the global ocean, but here they are just calibrated to average values. Despite this simplification, the model produces global patterns of biomass, production, and surface nutrients reasonably. There are however notable deviations, and these are important to keep in mind when the results are interpreted: 1) The model produces unrealistically high production in the Southern Ocean. This is due to the lack of iron as a nutrient,

480 which is known to be limiting production in the Southern Ocean (Bazzani et al., 2023). This results in overestimation of the biomass of phytoplankton and concomitantly the predators thereof, 2) as mentioned above, the model does not represent well large diatoms outside seasonal environments.

The evaluation of copepod global trait-distribution is challenging, with only a handful of global studies on copepod trait-distribution conducted ((Brun et al., 2016; Benedetti et al., 2023)). We compare our results (Fig. 13b) with the functional

485 traits identified in the global ocean in Benedetti et al. (2023), adopting the classification proposed by Brun et al. (2016), which categorizes cruise-current-feeding, current-feeding and cruise-feeding copepod species as active feeding copepods and ambush-feeding species as passive feeding copepods. Further, we use the annual habitat suitability index (HSI, (Benedetti et al., 2023)) as a proxy for the prevailing feeding strategies. Our results show that the highest ratio of active copepods is found in

the Southern Ocean (SO), North Pacific, and Arctic Ocean. This aligns with observations reporting the highest proportions of
490 current-cruise-feeding, current-feeding, and cruise-feeding species in these regions ((Benedetti et al., 2023)). Our model also
reproduces a lower fraction of active-feeding copepods in oligotrophic areas, such as the Pacific Equatorial band and the Indian
Ocean, which belong to the same regional categorization (Benedetti et al., 2023) and exhibit the highest proportions of ambush-
feeding species. The model predicts a higher ratio of passive feeders at temperate latitudes in the North Atlantic, North Pacific,
and South Pacific, where the mean annual habitat suitability index for ambush feeders is elevated. Conversely, a higher fraction
495 of active feeders populates most of the South Atlantic Ocean, except for a specific area where this fraction decreases. This
"green blob with the yellow ring" in the South Atlantic corresponds to a region with low nutrient levels (nitrogen and silica),
indicative of the prevalence of small unicellular generalists, which are preferentially consumed by passive-feeding copepods
due to their size and motility. The depletion of silica excludes the presence of diatoms, a preferred food source for active
feeders, which may explain the decrease in the fraction of active feeders in this region. The biomass of large copepods is lower
500 in oligotrophic regions and increases at higher latitudes, particularly in the Southern Ocean, North Atlantic and Northwest
Pacific. In contrast, the Northeast Pacific is nitrogen-depleted in the model (Fig. 11b), with lower unicellular plankton biomass
there (Fig. 7a,b), which limits the capacity of this region to sustain active copepods.

In the model design we have been mindful that overly complicated models are difficult to explain and are computationally
expensive. In this task, we have tried to target the Medawar zone (Medawar, 1967; Loehle, 1990) and made simplifying
505 assumptions that sometimes lead to limitations, some of which can be addressed in future versions. Apart from those already
mentioned, a stand out limitation is the unresolved behavioural trait of motility that is known to have significant consequences
on trophic and population dynamics in the plankton (Mariani et al., 2013; Kenitz et al., 2017; Pinti et al., 2022). While certain
aspects have been incorporated in the feeding mode parameterization of multicellular components, this has not been extended to
the unicellular components. Neither has vertical migration - either diurnal or seasonal been included – a behavior that amongst
510 other things, appears to play a significant role in the biological carbon pump (Hansen and Visser, 2016; Pinti et al., 2023a, b).
In some cases we have purposefully avoided modelling aspects of plankton ecology that are phenomenologically well known
but lack a mechanistic understanding. The underlying philosophy we pursue is to base all model descriptions on first principles
as much as possible (Andersen and Visser, 2023). In some cases the underlying trade-offs remain elusive. What, for instance is
the cost-benefit of calcifying plankton such as coccolithophres (Monteiro et al., 2016), and what mechanism provides diatoms a
515 faster cell division rate than other phototrophic plankton (Hansen and Visser, 2019)? Rather than introducing extra parameters
to fix these issues, we want to see how far a generalized model can come in explaining observed global patterns of ocean
plankton ecology. If the broad contours of these patterns can be explained, then future marine ecosystems under climate
change can be predicted with the same level of certainty.

Code and data availability. The code repository for this version of the framework is available via Zenodo at https://doi.org/10.5281/zenodo.
520 14280889 (Papapostolou (2025)). This version corresponds to the official release version 1.0 and includes the code used to generate all
figures in the manuscript https://doi.org/10.5281/zenodo.15856680. The code for the general framework and an actively developed version

of the code is also hosted on GitHub at https://github.com/Kenhasteandersen/NUMmodel, where full documentation is available through the wiki and help pages for all functions.

Author contributions. AP contributed the diatom model, collected and analyzed data for validation, conducted simulations and made all figures. KHA developed the general model framework. The manuscript was jointly written by AP and KHA with contributions from all co-authors.

Competing interests. The authors declare that they have no conflict of interest.

Acknowledgements. This publication was funded by the European Union (GA 101059915 BIOcean5D and GA 869383 ECOTIP), by the VKR Center of Excellence Ocean Life, by the Simon's Foundation grant 931976, and by the NFR project 334996 "Pelagic". Views and opinions expressed are however those of the authors only and do not necessarily reflect those of the European Union or the European Research Executive Agency (REA). Neither the European Union nor the granting authority can be held responsible for them. Thanks to Stephanie Dutkiewicz for hosting AP during a research stay at the Department of Earth, Atmospheric, and Planetary Sciences at the Massachusetts Institute of Technology, and for discussions on evaluation of global plankton models.

References

535   Andersen, K., Berge, T., Gonçalves, R., Hartvig, M., Heuschele, J., Hylander, S., Jacobsen, N., Lindemann, C., Martens, E., Neuheimer, A., Olsson, K., Palacz, A., Prowe, A., Sainmont, J., Traving, S., Visser, A., Wadhwa, N., and Kiørboe, T.: Characteristic Sizes of Life in the Oceans, from Bacteria to Whales, Annual Review of Marine Science, 8, 217–241, https://doi.org/10.1146/annurev-marine-122414-034144, 2016.

Andersen, K. H. and Visser, A.: From cell size and first principles to structure and function of unicellular plankton communities, Progress in
540   Oceanography, 213, 102 995, https://doi.org/10.1016/j.pocean.2023.102995, 2023.

Basu, S. and Mackey, K. R.: Phytoplankton as key mediators of the biological carbon pump: Their responses to a changing climate, Sustainability, 10, 869, https://doi.org/10.3390/su10030869, 2018.

Bazzani, E., Lauritano, C., and Saggiomo, M.: Southern Ocean iron limitation of primary production between past knowledge and future projections, Journal of Marine Science and Engineering, 11, 272, https://doi.org/10.3390/jmse11020272, 2023.

545   Behrenfeld, M. J. and Falkowski, P. G.: Photosynthetic rates derived from satellite-based chlorophyll concentration, Limnology and oceanography, 42, 1–20, https://doi.org/10.4319/lo.1997.42.1.0001, 1997.

Benedetti, F., Wydler, J., and Vogt, M.: Copepod functional traits and groups show divergent biogeographies in the global ocean, Journal of Biogeography, 50, 8–22, https://doi.org/10.1111/jbi.14512, 2023.

Benoiston, A.-S., Ibarbalz, F. M., Bittner, L., Guidi, L., Jahn, O., Dutkiewicz, S., and Bowler, C.: The evolution of diatoms
550   and their biogeochemical functions, Philosophical Transactions of the Royal Society B: Biological Sciences, 372, 20160 397, https://doi.org/10.1098/rstb.2016.0397, 2017.

Boyce, D. G., Frank, K. T., and Leggett, W. C.: From mice to elephants: overturning the 'one size fits all' paradigm in marine plankton food chains, Ecology Letters, 18, 504–515, https://doi.org/10.1111/ele.12434, 2015.

Boyd, P. W., Claustre, H., Levy, M., Siegel, D. A., and Weber, T.: Multi-faceted particle pumps drive carbon sequestration in the ocean,
555   Nature, 568, 327–335, https://doi.org/10.1038/s41586-019-1098-2, 2019.

Brett, M. T., Kainz, M. J., Taipale, S. J., and Seshan, H.: Phytoplankton, not allochthonous carbon, sustains herbivorous zooplankton production, Proceedings of the National Academy of Sciences, 106, 21 197–21 201, https://doi.org/10.1073/pnas.0904129106, 2009.

Bruggeman, J. and Bolding, K.: A general framework for aquatic biogeochemical models, Environmental Modelling & Software, 61, 249–265, https://doi.org/10.1016/j.envsoft.2014.04.002, 2014.

560   Brun, P., Payne, M. R., and Kiørboe, T.: Trait biogeography of marine copepods–an analysis across scales, Ecology Letters, 19, 1403–1413, https://doi.org/10.1111/ele.12688, 2016.

Brzezinski, M. A.: The Si: C: N ratio of marine diatoms: interspecific variability and the effect of some environmental variables 1, Journal of Phycology, 21, 347–357, https://doi.org/10.1111/j.0022-3646.1985.00347.x, 1985.

Cadier, M., Hansen, A. N., Andersen, K. H., and Visser, A. W.: Competition between vacuolated and mixotrophic unicellular plankton,
565   Journal of Plankton Research, 42, 425–439, https://doi.org/10.1093/plankt/fbaa025, 2020.

Castonguay, M., Plourde, S., Robert, D., Runge, J. A., and Fortier, L.: Copepod production drives recruitment in a marine fish, Canadian Journal of Fisheries and Aquatic Sciences, 65, 1528–1531, https://doi.org/10.1139/F08-126, 2008.

Chakraborty, S., Cadier, M., Visser, A. W., Bruggeman, J., and Andersen, K. H.: Latitudinal Variation in Plankton Traits and Ecosystem Function, Global Biogeochemical Cycles, 34, https://doi.org/10.1029/2020GB006564, 2020.

570 Chavez, F. P., Buck, K. R., Service, S. K., Newton, J., and Barber, R. T.: Phytoplankton variability in the central and eastern tropical Pacific, Deep Sea Research Part II: Topical Studies in Oceanography, 43, 835–870, https://doi.org/10.1016/0967-0645(96)00028-8, 1996.

De Roos, A. M., Schellekens, T., Van Kooten, T., Van De Wolfshaar, K., Claessen, D., and Persson, L.: Simplifying a physiologically structured population model to a stage-structured biomass model, Theoretical population biology, 73, 47–62, https://doi.org/10.1016/j.tpb.2007.09.004, 2008.

575 Durbin, A. G. and Durbin, E. G.: Seasonal changes in size frequency distribution and estimated age in the marine copepod Acartia hudsonica during a winter-spring diatom bloom in Narragansett Bay, Limnology and Oceanography, 37, 379–392, https://doi.org/10.4319/lo.1992.37.2.0379, 1992.

Endo, H., Ogata, H., and Suzuki, K.: Contrasting biogeography and diversity patterns between diatoms and haptophytes in the central Pacific Ocean, Scientific Reports, 8, 10 916, https://doi.org/10.1038/s41598-018-29039-9, 2018.

580 Evans, G. T. and Parslow, J. S.: A Model of Annual Plankton Cycles, Biological Oceanography, 3, 327–347, https://doi.org/10.1080/01965581.1985.10749478, 1985.

Fasham, M. J. R., Ducklow, H. W., and McKelvie, S. M.: A nitrogen-based model of plankton dynamics in the oceanic mixed layer, Journal of Marine Research, 48, 591–639, https://doi.org/10.1357/002224090784984678, 1990.

Fenchel, T.: Ecology of Protozoa: The biology of free-living phagotropic protists, Springer-Verlag, 2013.

585 Flynn, K. J., Stoecker, D. K., Mitra, A., Raven, J. A., Glibert, P. M., Hansen, P. J., Granéli, E., and Burkholder, J. M.: Misuse of the phytoplankton–zooplankton dichotomy: the need to assign organisms as mixotrophs within plankton functional types, Journal of Plankton Research, 35, 3–11, https://doi.org/10.1093/plankt/fbs062, 2013.

Follows, M. J., Dutkiewicz, S., Grant, S., and Chisholm, S. W.: Emergent Biogeography of Microbial Communities in a Model Ocean, Science, 315, 1843–1846, https://doi.org/10.1126/science.1138544, publisher: American Association for the Advancement of Science
590 Section: Report, 2007.

Hamm, C. E., Merkel, R., Springer, O., Jurkojc, P., Maier, C., Prechtel, K., and Smetacek, V.: Architecture and material properties of diatom shells provide effective mechanical protection, Nature, 421, 841–843, https://doi.org/10.1038/nature01416, 2003.

Hansen, A. N. and Visser, A. W.: Carbon export by vertically migrating zooplankton: an optimal behavior model, Limnology and Oceanography, 61, 701–710, https://doi.org/10.1002/lno.10249, 2016.

595 Hansen, A. N. and Visser, A. W.: The seasonal succession of optimal diatom traits, Limnology and Oceanography, 64, 1442–1457, https://doi.org/10.1002/lno.11126, 2019.

Hansen, T. F., Canfield, D. E., Andersen, K. H., and Bjerrum, C. J.: The unicellular NUM v. 0.91: A trait-based plankton model evaluated in two contrasting biogeographic provinces, Geoscientific Model Development Discussions, 2024, 1–39, https://doi.org/10.5194/gmd-2024-53, 2024.

600 Heath, M. R., Speirs, D. C., and Steele, J. H.: Understanding patterns and processes in models of trophic cascades, Ecology letters, 17, 101–114, https://doi.org/10.1111/ele.12200, 2014.

Hillebrand, H., Acevedo-Trejos, E., Moorthi, S. D., Ryabov, A., Striebel, M., Thomas, P. K., and Schneider, M.-L.: Cell size as driver and sentinel of phytoplankton community structure and functioning, Functional Ecology, 36, 276–293, https://doi.org/10.1111/1365-2435.13986, 2022.

605 Humes, A. G.: How many copepods?, Hydrobiologia, 292, 1–7, https://doi.org/10.1007/BF00229916, 1994.

Kenitz, K. M., Visser, A. W., Mariani, P., and Andersen, K. H.: Seasonal succession in zooplankton feeding traits reveals trophic trait coupling, Limnology and Oceanography, 62, 1184–1197, https://doi.org/10.1002/lno.10494, 2017.

Kiørboe, T., Møhlenberg, F., and Hamburger, K.: Bioenergetics of the planktonic copepod Acartia tonsa: relation between feeding, egg pro-
duction and respiration, and composition of specific dynamic action, Mar Ecol Prog Ser, 26, 85–97, https://doi.org/10.3354/meps026085,
1985.

Kiørboe, T. and Hirst, A. G.: Shifts in Mass Scaling of Respiration, Feeding, and Growth Rates across Life-Form Transitions in Marine
Pelagic Organisms., The American Naturalist, 183, E118–E130, https://doi.org/10.1086/675241, publisher: The University of Chicago
Press, 2014.

Kudela, R. M., Banas, N. S., Barth, J. A., Frame, E. R., Jay, D. A., Largier, J. L., Lessard, E. J., Peterson, T. D., and Vander Woude, A. J.:
New insights into the controls and mechanisms of plankton productivity in coastal upwelling waters of the northern California Current
System, Oceanography, 21, 46–59, https://doi.org/10.5670/oceanog.2008.04, 2008.

Lee Chen, Y.-l., Chen, H.-Y., Tuo, S.-h., and Ohki, K.: Seasonal dynamics of new production from Trichodesmium N2 fixa-
tion and nitrate uptake in the upstream Kuroshio and South China Sea basin, Limnology and Oceanography, 53, 1705–1721,
https://doi.org/10.4319/lo.2008.53.5.1705, 2008.

Lenton, T. M. and Watson, A. J.: Redfield revisited: 1. Regulation of nitrate, phosphate, and oxygen in the ocean, Global biogeochemical
cycles, 14, 225–248, https://doi.org/10.1029/1999GB900065, 2000.

Loehle, C.: A guide to increased creativity in research: inspiration or perspiration?, Bioscience, 40, 123–129,
https://doi.org/10.2307/1311345, 1990.

López, E. and Anadón, R.: Copepod communities along an Atlantic Meridional Transect: Abundance, size structure, and grazing rates, Deep
Sea Research Part I: Oceanographic Research Papers, 55, 1375–1391, https://doi.org/10.1016/j.dsr.2008.05.012, 2008.

Mackey, D., Blanchot, J., Higgins, H., and Neveux, J.: Phytoplankton abundances and community structure in the equatorial Pacific, Deep
Sea Research Part II: Topical Studies in Oceanography, 49, 2561–2582, https://doi.org/10.1016/S0967-0645(02)00048-6, 2002.

Marañón, E., Holligan, P. M., Varela, M., Mouriño, B., and Bale, A. J.: Basin-scale variability of phytoplankton biomass, production and
growth in the Atlantic Ocean, Deep Sea Research Part I: Oceanographic Research Papers, 47, 825–857, https://doi.org/10.1016/S0967-
0637(99)00087-4, 2000.

Mariani, P., Andersen, K. H., Visser, A. W., Barton, A. D., and Kiørboe, T.: Control of plankton seasonal succession by adaptive grazing,
Limnology and Oceanography, 58, 173–184, https://doi.org/10.4319/lo.2013.58.1.0173, 2013.

Martínez-Vicente, V., Evers-King, H., Roy, S., Kostadinov, T. S., Tarran, G. A., Graff, J. R., Brewin, R. J., Dall'Olmo, G., Jackson, T.,
Hickman, A. E., et al.: Intercomparison of ocean color algorithms for picophytoplankton carbon in the ocean, Frontiers in Marine Science,
4, 378, https://doi.org/10.3389/fmars.2017.00378, 2017.

Medawar, P. B.: The art of the soluble, Routledge, https://doi.org/10.4324/9781003221036, 1967.

Millette, N. C., Gast, R. J., Luo, J. Y., Moeller, H. V., Stamieszkin, K., Andersen, K. H., Brownlee, E. F., Cohen, N. R., Duhamel,
S., Dutkiewicz, S., et al.: Mixoplankton and mixotrophy: future research priorities, Journal of Plankton Research, 45, 576–596,
https://doi.org/10.1093/plankt/fbad020, 2023.

Mitra, A., Castellani, C., Gentleman, W. C., Jónasdóttir, S. H., Flynn, K. J., Bode, A., Halsband, C., Kuhn, P., Licandro, P., Agersted,
M. D., et al.: Bridging the gap between marine biogeochemical and fisheries sciences; configuring the zooplankton link, Progress in
Oceanography, 129, 176–199, https://doi.org/10.1016/j.pocean.2014.04.025, 2014.

Monteiro, F. M., Bach, L. T., Brownlee, C., Bown, P., Rickaby, R. E., Poulton, A. J., Tyrrell, T., Beaufort, L., Dutkiewicz, S., Gibbs, S., et al.:
Why marine phytoplankton calcify, Science Advances, 2, e1501 822, https://doi.org/10.1126/sciadv.1501822, 2016.

645 Moriarty, R., Buitenhuis, E., Le Quéré, C., and Gosselin, M.-P.: Distribution of known macrozooplankton abundance and biomass in the global ocean, Earth System Science Data, 5, 241–257, https://doi.org/10.5194/essd-5-241-2013, 2013.

Nowicki, M., DeVries, T., and Siegel, D. A.: Quantifying the carbon export and sequestration pathways of the ocean's biological carbon pump, Global Biogeochemical Cycles, 36, e2021GB007 083, https://doi.org/10.1029/2021GB007083, 2022.

Ocean Productivity: Ocean Productivity Home Page, http://sites.science.oregonstate.edu/ocean.productivity/index.php, accessed: 2024-04-
650 25, 2024.

Pančić, M., Torres, R. R., Almeda, R., and Kiørboe, T.: Silicified cell walls as a defensive trait in diatoms, Proceedings of the Royal Society B, 286, 20190 184, https://doi.org/10.1098/rspb.2019.0184, 2019.

Papapostolou, A.: Computational library for the Nutrient-Unicellular-Multicellular plankton modeling framework (code), https://doi.org/10.5281/zenodo.14280889, 2025.

655 Pinti, J., Visser, A. W., Serra-Pompei, C., Andersen, K. H., Ohman, M. D., and Kiørboe, T.: Fear and loathing in the pelagic: How the seascape of fear impacts the biological carbon pump, Limnology and Oceanography, 67, 1238–1256, https://doi.org/10.1002/lno.12073, 2022.

Pinti, J., DeVries, T., Norin, T., Serra-Pompei, C., Proud, R., Siegel, D. A., Kiørboe, T., Petrik, C. M., Andersen, K. H., Brierley, A. S., et al.: Model estimates of metazoans' contributions to the biological carbon pump, Biogeosciences, 20, 997–1009, https://doi.org/10.5194/bg-
660 20-997-2023, 2023a.

Pinti, J., Jónasdóttir, S. H., Record, N. R., and Visser, A. W.: The global contribution of seasonally migrating copepods to the biological carbon pump, Limnology and Oceanography, 68, 1147–1160, https://doi.org/10.1002/lno.12335, 2023b.

Reagan, J. R., Boyer, T., García, H., Locarnini, R., Baranova, O., Bouchard, C., Cross, S., Mishonov, A., Paver, C., Seidov, D., and Wang, Zhankunand Dukhovskoy, D.: World Ocean Atlas 2023, NOAA National Centers for Environmental Information Dataset, https://www.
665 ncei.noaa.gov/archive/accession/0270533, [Accessed 26-07-2024], 2023.

Record, N., Pershing, A., and Maps, F.: Emergent copepod communities in an adaptive trait-structured model, Ecological modelling, 260, 11–24, https://doi.org/10.1016/j.ecolmodel.2013.03.018, 2013.

Rodríguez-Ramos, T., Marañón, E., and Cermeño, P.: Marine nano- and microphytoplankton diversity: redrawing global patterns from sampling-standardized data, Global Ecology and Biogeography, 24, 527–538, https://doi.org/10.1111/geb.12274, 2015.

670 Rombouts, I., Beaugrand, G., Ibañez, F., Gasparini, S., Chiba, S., and Legendre, L.: Global latitudinal variations in marine copepod diversity and environmental factors, Proceedings of the Royal Society B: Biological Sciences, 276, 3053–3062, https://doi.org/10.1098/rspb.2009.0742, publisher: Royal Society, 2009.

Ryther, J. H.: Photosynthesis and Fish Production in the Sea, Science, 166, 72–76, https://doi.org/10.1126/science.166.3901.72, 1969.

Serra-Pompei, C., Hagstrom, G. I., Visser, A. W., and Andersen, K. H.: Resource limitation determines temperature response
675 of unicellular plankton communities, Limnology and Oceanography, 64, 1627–1640, https://doi.org/10.1002/lno.11140, _eprint: https://aslopubs.onlinelibrary.wiley.com/doi/pdf/10.1002/lno.11140, 2019.

Serra-Pompei, C., Soudijn, F., Visser, A. W., Kiørboe, T., and Andersen, K. H.: A general size- and trait-based model of plankton communities, Progress in Oceanography, 189, 102 473, https://doi.org/10.1016/j.pocean.2020.102473, 2020.

Serra-Pompei, C., Ward, B. A., Pinti, J., Visser, A. W., Kiørboe, T., and Andersen, K. H.: Zooplankton trophic dynamics drive carbon export
680 efficiency, preprint, Ecology, https://doi.org/10.1101/2021.03.08.434455, 2021.

Serra-Pompei, C., Ward, B. A., Pinti, J., Visser, A. W., Kiørboe, T., and Andersen, K. H.: Linking plankton size spectra and community composition to carbon export and its efficiency, Global Biogeochemical Cycles, https://doi.org/10.1029/2021GB007275, 2022.

Silsbe, G. M., Behrenfeld, M. J., Halsey, K. H., Milligan, A. J., and Westberry, T. K.: The CAFE model: A net production model for global ocean phytoplankton, Global Biogeochemical Cycles, 30, 1756–1777, https://doi.org/10.1002/2016GB005521, 2016.

685 Steinberg, D. K. and Landry, M. R.: Zooplankton and the Ocean Carbon Cycle, Annual Review of Marine Science, 9, 413–444, https://doi.org/10.1146/annurev-marine-010814-015924, 2017.

Stock, C. A., Dunne, J. P., and John, J. G.: Global-scale carbon and energy flows through the marine planktonic food web: An analysis with a coupled physical–biological model, Progress in Oceanography, 120, 1–28, https://doi.org/10.1016/j.pocean.2013.07.001, 2014.

Tanioka, T., Larkin, A. A., Moreno, A. R., Brock, M. L., Fagan, A. J., Garcia, C. A., Garcia, N. S., Gerace, S. D., Lee, J. A., Lomas, M. W.,
690 et al.: Global ocean particulate organic phosphorus, carbon, oxygen for respiration, and Nitrogen (GO-POPCORN), Scientific data, 9, 688, https://doi.org/10.1038/s41597-022-01809-1, 2022.

Thingstad, T. F., Øvreås, L., Egge, J. K., Løvdal, T., and Heldal, M.: Use of non-limiting substrates to increase size; a generic strategy to simultaneously optimize uptake and minimize predation in pelagic osmotrophs?, Ecology Letters, 8, 675–682, https://doi.org/10.1111/j.1461-0248.2005.00768.x, 2005.

695 Tréguer, P., Bowler, C., Moriceau, B., Dutkiewicz, S., Gehlen, M., Aumont, O., Bittner, L., Dugdale, R., Finkel, Z., Iudicone, D., Jahn, O., Guidi, L., Lasbleiz, M., Leblanc, K., Levy, M., and Pondaven, P.: Influence of diatom diversity on the ocean biological carbon pump, Nature Geoscience, 11, 27–37, https://doi.org/10.1038/s41561-017-0028-x, bandiera_abtest: a Cg_type: Nature Research Journals Number: 1 Primary_atype: Reviews Publisher: Nature Publishing Group Subject_term: Biogeochemistry;Carbon cycle;Marine biology;Ocean sciences Subject_term_id: biogeochemistry;carbon-cycle;marine-biology;ocean-sciences, 2018.

700 Turner, E. L., Bruesewitz, D. A., Mooney, R. F., Montagna, P. A., McClelland, J. W., Sadovski, A., and Buskey, E. J.: Comparing performance of five nutrient phytoplankton zooplankton (NPZ) models in coastal lagoons, Ecological Modelling, 277, 13–26, https://doi.org/10.1016/j.ecolmodel.2014.01.007, 2014.

Turner, J. T.: Zooplankton fecal pellets, marine snow, phytodetritus and the ocean's biological pump, Progress in Oceanography, 130, 205–248, https://doi.org/10.1016/j.pocean.2014.08.005, 2015.

705 Vargas, C. A., Escribano, R., and Poulet, S.: Phytoplankton food quality determines time windows for successful zooplankton reproductive pulses, Ecology, 87, 2992–2999, https://doi.org/10.1890/0012-9658(2006)87[2992:PFQDTW]2.0.CO;2, 2006.

Verity, P. G. and Smetacek, V.: Organism life cycles, predation, and the structure of marine pelagic ecosystems, Marine Ecology Progress Series, 130, 277–293, https://doi.org/10.3354/meps130277, 1996.

Vidal, J. and Smith, S. L.: Biomass, growth, and development of populations of herbivorous zooplankton in the southeastern Bering Sea
710 during spring, Deep Sea Research Part A. Oceanographic Research papers, 33, 523–556, https://doi.org/10.1016/0198-0149(86)90129-9, 1986.

Visser, A., Almgren, A., and Kandylas, A.: SISSOMA (v1): modelling marine aggregate dynamics from production to export, preprint, Modelling, https://doi.org/10.5194/egusphere-2024-2520, 2024.

Waite, R., Beveridge, M., Brummett, R., Castine, S., Chaiyawannakarn, N., Kaushik, S., Mungkung, R., Nawapakpilai, S., and Phillips, M.:
715 Improving productivity and environmental performance of aquaculture, WorldFish, https://coilink.org/20.500.12592/b36ckm, 2014.

Ward, B. A. and Follows, M. J.: Marine mixotrophy increases trophic transfer efficiency, mean organism size, and vertical carbon flux, Proceedings of the National Academy of Sciences, 113, 2958–2963, https://doi.org/10.1073/pnas.1517118113, 2016.

Ward, B. A., Wilson, J. D., Death, R. M., Monteiro, F. M., Yool, A., and Ridgwell, A.: EcoGEnIE 1.0: plankton ecology in the cGEnIE Earth system model, Geoscientific Model Development, 11, 4241–4267, https://doi.org/10.5194/gmd-11-4241-2018, publisher: Coperni-
720 cus GmbH, 2018.

Westberry, T., Behrenfeld, M. J., Siegel, D. A., and Boss, E.: Carbon-based primary productivity modeling with vertically resolved photoac-
climation, Global Biogeochemical Cycles, 22, https://doi.org/10.1029/2007GB003078, 2008.

Wirtz, K. W.: Who is eating whom? Morphology and feeding type determine the size relation between planktonic predators and their ideal
prey, Marine Ecology Progress Series, 445, 1–12, https://doi.org/10.3354/meps09502, 2012.

Appendix B: Model equations and parameters

Equations and parameters for unicellular plankton are in Tables B1 and B2, for copepods in Tables B3 and B4, and parameters for POM in Table B5.

B1 Diatom membrane fraction

Let r be the radius of the entire cell including the outer membrane, r_{vac} the vacuole radius, ν_{vac} the fraction of the cell volume occupied by the vacuole, ρ the cell density, and δ the thickness of each membrane (see fig. 2). The total cell volume is:

$$V = \frac{4}{3}\pi r^3 \Leftrightarrow r = \left(\frac{3}{4\pi}V\right)^{1/3} \tag{B1}$$

The vacuole volume is:

$$V_{\mathrm{vac}} = \frac{4}{3}\pi r_{\mathrm{vac}}^3 \Leftrightarrow \nu_{\mathrm{vac}} \frac{V_{\mathrm{vac}}}{V} = \frac{r_{\mathrm{vac}}^3}{r^3} \Leftrightarrow r_{\mathrm{vac}} = r\nu_{\mathrm{vac}}^{1/3} \tag{B2}$$

The volume of the membranes is:

$$V_{\mathrm{m}} = \underbrace{\frac{4}{3}\pi(r^3 - (r-\delta)^3)}_{\text{outer membrane}} + \underbrace{\frac{4}{3}\pi((r_{\mathrm{vac}}+\delta)^3 - r_{\mathrm{vac}}^3)}_{\text{inner membrane}} \tag{B3}$$

The Taylor series expansion of $f(x) = r^3 - (r-x)^3$ around $\delta = 0$ is $3r^2\delta$.

The approximation for the volume of membranes is then:

$$V_{\mathrm{m}} \approx 4\pi r^2 \delta + 4\pi r_{\mathrm{vac}^2}\delta \overset{\text{(B2)}}{=} 4\pi\delta(1 + \nu_{\mathrm{vac}}^{2/3})r^2 \tag{B4}$$

Assuming the vacuole density to be 0, the mass of the cell is:

$$m = \rho(V - V_{\mathrm{vac}}) \overset{\text{(B2)}}{=} \rho V(1 - \nu_{\mathrm{vac}}) \Leftrightarrow r = \left(\frac{3}{4\pi}\frac{m}{\rho}\frac{1}{1-\nu_{\mathrm{vac}}}\right)^{1/3} \tag{B5}$$

The membrane fraction of the cell's mass is then:

$$\begin{aligned}
\nu_{\mathrm{m}} = \frac{\rho V_{\mathrm{m}}}{m} &\overset{\text{(B4),(B5)}}{=} \frac{4\pi\delta(1+\nu_{\mathrm{vac}}^{2/3})r^2}{4/3\pi(1-\nu_{\mathrm{vac}}r^3)} \\
&= 3\frac{\delta}{r}\frac{1+\nu_{\mathrm{vac}}^{2/3}}{1-\nu_{\mathrm{vac}}} \overset{\text{(B5)}}{=} 3\delta\left(\frac{4\pi}{3}\right)^{1/3}\left(\frac{m}{\rho}\right)^{-1/3}\frac{1+\nu_{\mathrm{vac}}^{2/3}}{(1-\nu_{\mathrm{vac}})^{2/3}} \\
&= 6^{2/3}\pi^{1/3}\delta\left(\frac{m}{\rho}\right)^{-1/3}\frac{1+\nu_{\mathrm{vac}}^{2/3}}{(1-\nu_{\mathrm{vac}})^{2/3}}
\end{aligned} \tag{B6}$$

and the active biomass fraction is: $\nu = 1 - \nu_{\mathrm{m}}$.

Table B1: Equations for the unicellular models (generalists and diatoms)

Description	Equation
Geometry	
Radius	$r = \left(\dfrac{3}{4\pi} \dfrac{m}{\rho} \dfrac{1}{1 - v_{\text{vac}}} \right)^{1/3}$
Active biomass fraction	$\nu = 1 - \left[6^{2/3} \pi^{1/3} \delta \left(\dfrac{m}{\rho} \right)^{-1/3} \dfrac{1 + \nu_{vac}^{2/3}}{(1 - \nu_{vac})^{2/3}} \right]$
Affinities	
Diffusive affinity	$a_{\text{D}} = \dfrac{\alpha_{\text{N}} r^{-2}}{1 + (\frac{r}{r_{\text{N*}}})^{-2}} \dfrac{1}{1 - v_{\text{vac}}}$
Light affinity	$a_{\text{L}} = \dfrac{\alpha_{\text{L}}}{r} \left[1 - \exp\left(-\dfrac{r}{r_{\text{L*}}} \right) \right] \dfrac{1 - \nu}{1 - v_{\text{vac}}}$
Food affinity	$a_{\text{F}} = \alpha_{\text{F}}$
Metabolism	
Max. synthesis rate	$j_{\max} = \alpha_{\max}(1 - \nu)$
Basal metabolism	$j_{\text{R}} = \alpha_{\text{R}} \alpha_{\max}$
Passive losses	$j_{\text{passive}} = c_{\text{passive}}/r$
Resource encounter	
Nutrient encounter rate	$j_{\text{enc}.X} = a_{\text{D}} \rho_{\text{C}:X} N$ with $X \in \{\text{N}, \text{DOC}, \text{Si}\}$
Light encounter rate	$j_{\text{enc.L}} = \epsilon_{\text{L}} a_{\text{L}} L$
Food encounter rate	$j_{\text{enc.F}} = \epsilon_{\text{F}} j_{\text{Fmax}} \dfrac{a_F F}{a_F j_{\text{Fmax}} + a_{\text{F}} F}$ with $j_{\text{Fmax}} = \dfrac{c_{\text{F}}}{r}$
Synthesis	
Total potential nitrogen uptake	$j_{\text{enc.Ntot}} = j_{\text{enc.N}} + j_{\text{enc.F}} - j_{\text{passive}}$
Total potential carbon uptake	$j_{\text{enc.Ctot}} = j_{\text{enc.L}} + j_{\text{enc.F}} + j_{\text{enc.DOC}}$ $- j_{\text{resp}} - j_{\text{passive}}$
Uptake based on Liebig's Law	$j_{\text{lieb}} = \min\{ j_{\max}, j_{\text{enc.N}}, j_{\text{enc.L}} - j_{\text{resp}}, j_{\text{enc.Si}} \}$
Total growth	$j_{\text{tot}} = f j_{\max}, \; f = \frac{j_{\text{lieb}}}{j_{\text{lieb}} + j_{\max}}$
Effective food uptake	$j_{\text{F}} = \begin{cases} \max\{0, j_{\text{F}} - (j_{\text{lieb}} - f j_{\max})\} \\ \max\{0, j_{\text{F}}\}, j_{\text{lieb}} < 0 \end{cases}$
Effective light uptake	$j_{\text{L}} = j_{\text{enc.L}} - \max[0, \min\{ j_{\text{Ctot}}$ $- (j_{\text{enc.F}} - j_{\text{F}} - j_{\text{tot}}), j_{\text{enc.L}}\}]$
Total effective nitrogen uptake	$j_{\text{Ntot}} = J_{\text{N}} + j_{\text{F}} - j_{\text{passive}}$
Total effective carbon uptake	$j_{\text{Ctot}} = j_{\text{L}} + J_{\text{DOC}} + j_{\text{F}}$ $- j_{\text{resp}} - j_{\text{passive}}$

Losses

Food assimilation losses

$$j_{\text{F.loss}} = \underbrace{\frac{1 - \epsilon_{\text{F}}}{\epsilon_{\text{F}}} j_{\text{F}}}_{\text{Sloppy feeding loss}}$$

Nitrogen losses

$$j_{\text{N.loss}} = j_{\text{F.loss}} + j_{\text{loss.passive}}$$
$$+ \max\{0, j_{\text{Ntot}} - j_{\text{tot}}\}$$

Carbon losses

$$j_{\text{C.loss}} = j_{\text{F.loss}} + \underbrace{\frac{1 - \epsilon_{\text{L}}}{\epsilon_{\text{L}}} j_{\text{L}}}_{\text{Photouptake loss}}$$

$$+ \max\{0, j_{\text{Ctot}} - j_{\text{tot}}\} + j_{\text{passive}}$$

[a] Only for diatoms

Table B2. Parameters for the unicellular model. All parameters from Andersen and Visser (2023) unless noted. Values in parentheses are for diatoms. Temperature corrections are given with Q_{10} regulation (18).

Symbol	Description	Value & Unit	Reference
General parameters			
$\rho_{C:N}$	C:N mass ratio of cell	5.68	
$\rho_{C:Si}$	C:Si ratio of cell	(3.4)	
ν_{vac}	Vacuole fraction	0 (0.6)	
ρ	Carbon density	$0.4 \times 10^{-6} \mu g\ C\ \mu m^{-1}$	
δ	Cell wall thickness	$0.05\ \mu m$	
Resource uptakes:			
α_F	Food affinity scaling factor	$0.018\ (0)\ L\mu g\ C^{-1}d^{-1}$	
c_F	Max phagotrophy coef.	$30\ \mu m/d$	
α_L	Light affinity scaling factor	0.3	
r_L^*	Light aff. cross-over	$7.5\ \mu m$	
α_N	Nutrient affinity scaling factor	$0.972\,Q_{1.5}(T)\ Ld^{-1}(\mu g\ C)^{-1}\mu m^2$	
r_N^*	Diffusive aff. cross-over	$0.4\ \mu m$	
Metabolism:			
α_{max}	Maximum synthesis rate	$1.5\,Q_2(T)\ d^{-1}$	
α_R	Basal resp. coef.	$0.03\,Q_2(T)$	
ϵ_L	Light uptake efficiency	0.8	
ϵ_F	Food assimilation efficiency	0.8	
β	Preferred pred:prey mass ratio	500	
σ	Feeding range	1.30	
β_N	Uptake cost of N	$0.3\ g_C/g_N$	
β_{DOC}	Uptake cost of DOC	0.3	
β_{Si}	Uptake cost of Si	$0(0.3\ g_C/g_{Si})$	
β_L	Uptake cost of CO_2	0.08	
β_F	Uptake cost of feeding	0.3 (0)	
β_g	Synthesis cost	0.2	
Losses:			
μ_2	quadratic mortality coefficient	$0.004\ (\mu g\ C\ L^{-1})^{-1}$	
$c_{passive}$	passive leakage coef.	0.03	
p	Vulnerability	1 (0.2)	

Table B3. Equations for the copepod growth and mortality model. Subscript s refers to the stage within the population and S is the adult stage. All variables are in dimensions of per time, except J_{in} which is biomass per time.

Description	Equation
Maximum consumption	$j_{\mathrm{Fmax}.s} = h m_s^n$
Available energy	$j_{\mathrm{avail}.s} = \epsilon j_{\mathrm{F}.s} - j_{\mathrm{resp}.s}$
Respiration	$j_{\mathrm{resp}.s} = k_{\mathrm{R}} \epsilon j_{\mathrm{Fmax}.s} + k_{\mathrm{SDA}} j_{\mathrm{F}.s}$ [b]
Biomass growth	$\max\{0, j_{\mathrm{avail}.s}\}$
Growth and reproductive flux	$J_{\mathrm{in}.s} = \begin{cases} \epsilon_{\mathrm{r}} g_S B_S, & s = 1 \\ j_{\mathrm{out},s-1} B_{s-1}, & s > 1 \end{cases}$
Somatic growth rate	$j_{\mathrm{out}.s} = \begin{cases} \frac{g_s - \mu_s}{1 - (m_s^- / m_s^+)^{1 - \mu_s / g_s}} \ [a], & s < S \\ 0, & s = S \end{cases}$
Starvation mortality	$\mu_{\mathrm{st}.s} = \min\{0, j_{\mathrm{avail}.s}\}$

[a] m_s^- / m_s^+ is the ratio between the lower and upper size of a size class; see Fig. C1.

[b] The formulation of respiration is slightly revised from the original formulation in Serra-Pompei et al. (2020). It consists of two terms: a fixed basal respiration that is proportional to the maximum respiration and a "specific dynamics action" that is proportional to consumption.

Table B4. Parameters for the copepod model. All parameters are from Serra-Pompei et al. (2022) except where noted.

Symbol	Description	Value		Unit
h	Max. consumption coef.	$0.29 Q_2(T)$	$0.97 Q_2(T)$	
ϵ_{F}	Assimilation eff.		0.67	
k_{R}	Basal metabolism coef.		$0.01 Q_2(T)$ [a]	$\mu\,\mathrm{g\ C}^{1/4}\mathrm{day}^{-1}$
k_{SDA}	Specific dyn. action coef.		0.16	
β	Preferred pred:prey mass ratio	100	10000	
σ	Size range pref.	1	1.5	
q	Clearance rate exponent		0.75	
α_{F}	Clearance rate coef.	0.29	0.97	$\mathrm{l}\cdot\mu\,\mathrm{g\ C}^{1/4}\mathrm{day}^{-1}$
m_{egg}	Offspring mass		$0.01 m_S$	
ϵ_{r}	Reproductive efficiency		0.25	
p	Vulnerability	0.2	1	

[a] This value represents the starvation metabolism. Following Kiørboe et al. (1985) the starvation metabolism is approximately 18% of the standard metabolism, which is approx. 20% of max metabolism. This gives a very small value of $k_{\mathrm{R}} = 0.006$, which implies that copepods can survive a long time. We increase the value to $k_{\mathrm{R}} = 0.01$ such that large copepods can survive approx. 200 days which is sufficient to surve the winter at high latitudes.

Table B5. Parameters involved in POM and nutrient cycling

Symbol	Description	Value & unit
r_{POM}	Remineralization rate	$0.07\,Q_2(T)\ \mathrm{day}^{-1}$
γ_2	Frac. of virulysis to POM	0.5
γ_{HTL}	Frac. of HTL mortality to POM	0.5
γ_{F}	Frac. of feeding losses to POM	0.1
p	Palatability	0.1

Appendix C: Computational grid for size groups
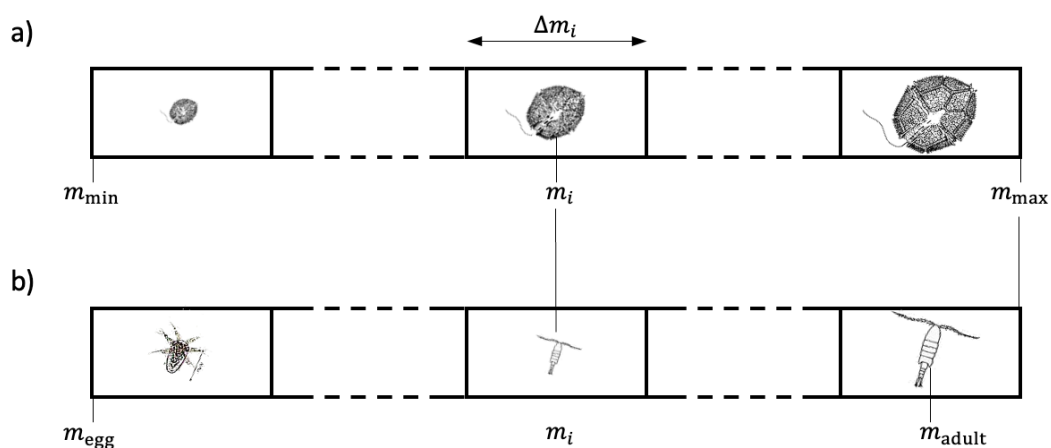
Figure C1. Specification of the computational grid used for unicellular organisms (a) and multicellular organisms (b). The grid for unicellular plankton contain n size groups in the range from m_{min} and m_{max}. Each size group is defined by its central mass (geometric mean) m_i. For multicellular plankton the grid for each group is from m_{egg}. The last size group has the central mass m_{adult}. This means that copepods actually becomes adult at smaller mass than m_{adult}, and that the last size group spans a range of masses.

Appendix D: Predation kernel

The effective prey preference function θ_{ij} between size classes of predators i and prey j should deal with the different width's of size classes depending on the size grid spacing. Following Andersen and Visser (2023) this is calculated by integrating over the prey size preference (Eq. 1). The encountered prey in size class j by all predators in class i is:

$$E_{ij} = \int\limits_{m_i^-}^{m_i^+} a_{\mathrm{F}} m \int\limits_{m_j^-}^{m_j^+} \phi(m,w) B(w)\,\mathrm{d}w\, B(m)/m\,\mathrm{d}m, \tag{D1}$$

where m_i^- and m_i^+ represent the upper an lower bounds of size class i. $B(m)$ represents the normalized biomass spectrum. We assume a Sheldon distribution, i.e., $B(m) \propto m^{-1}$. With the discrete prey and predator groups we can write the encountered food as:

$$E_{ij} = a_{\mathrm{F}} m_i \theta_{ij} B_j N_i \tag{D2}$$

Where B_j is the total biomass in class j, $B_j = \int B(w)\,\mathrm{d}w$ and N_i is the total abundance of predators $N_i = \int B(m)/m\,\mathrm{d}m$. Equating the two terms and isolating θ_{ij} gives:

$$\theta_{ij} = \frac{\sqrt{\Delta}}{(\Delta-1)\log(\Delta)}$$
$$\left[\left(\frac{1}{2}s\left(e^{-\frac{\log^2\left(\frac{\Delta z}{\beta}\right)}{s}} + e^{-\frac{\log^2\left(\frac{\beta\Delta}{z}\right)}{s}} - 2e^{-\frac{\log^2\left(\frac{z}{\beta}\right)}{s}}\right) - \right.$$
$$\frac{1}{2}\sqrt{\pi}\sqrt{s}\left(\log\left(\frac{\Delta z}{\beta}\right)\mathrm{erf}\left(\frac{\log(\beta)-\log(\Delta z)}{\sqrt{s}}\right) + \log\left(\frac{\beta\Delta}{z}\right)\mathrm{erf}\left(\frac{\log(z)-\log(\beta\Delta)}{\sqrt{s}}\right) + \right.$$
$$\left.\left.\left.\log\left(\frac{z}{\beta}\right)\mathrm{erf}\left(\frac{\log\left(\frac{z}{\beta}\right)}{\sqrt{s}}\right)\right)\right)\right] \tag{D3}$$

where $s = 2\sigma^2$ and $z = m_i/m_j$ and $\Delta = m^+/m^-$. In this way θ_{ij} represent the total preference of size class i and j, including a compensation for the width of size classes and the preference p_{kl} between predator from group k on group l (from Eq. 1). Technically the preference should be expressed as θ_{klij} but the dependence on the group preferences is suppressed to improve readability.

Appendix E: Data sources and processing

765 **E1   POC biomass: GOPOPCORN**

GO-POPCORN v2 consists of samples from 12 cruises from 2011 to 2020. We used POCavg_uM that range between 0.7 and 30μm. We compare the POC data with all plankton and detritus particles with a radius between 0.35-15 μm at the same coordinates, month and depth.

E2   Picophytoplankton biomass

770 We export the insitu phytoplankton biomass (Prochlorococcus, Synechococcus and Picoeukaryotic) at different transects and chlorophyll-a (depth-averaged between 0-10m and ignoring the deeper samples to match satellite measurements), that where measured at different months (ref. "Intercomparison of Ocean Color Algorithms from Picophytoplankton Carbon in the Ocean"). The cell counts were from water samples from up to 200m depth, between 1997 and 2014. Insitu data are compared to the models output at the top layer.
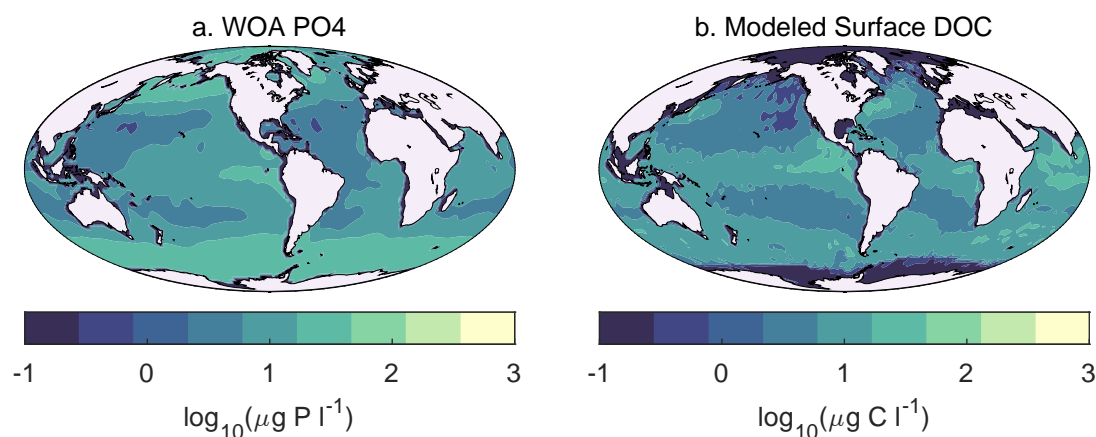
Figure E1. Annual mean concentrations of (a) phosphate (μg P l^{-1}) from World Ocean Atlas and (b) dissolved organic carbon (μg Si l^{-1}) at top 5m.
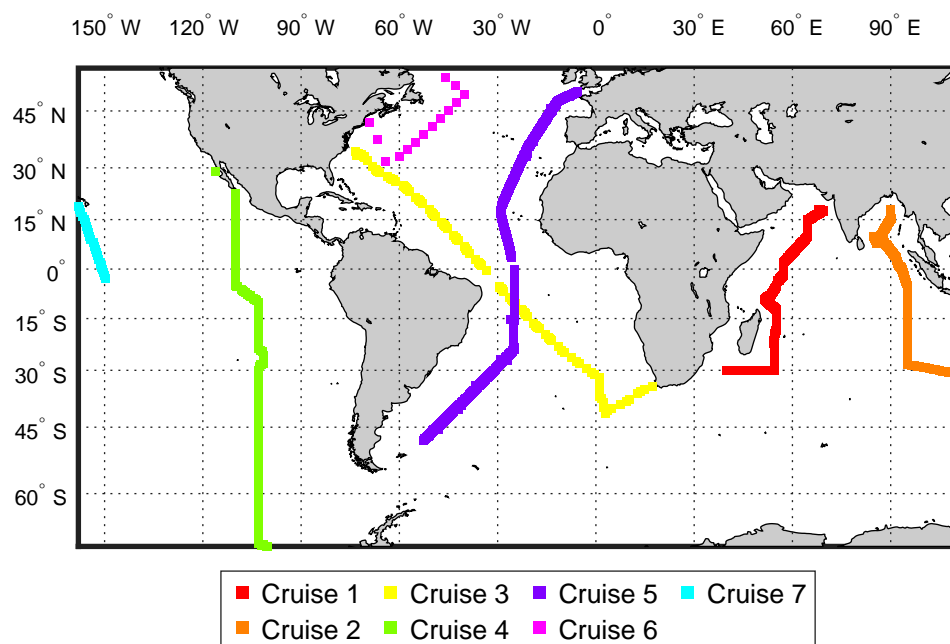
Figure E2. GOPOPCORN Cruises transects
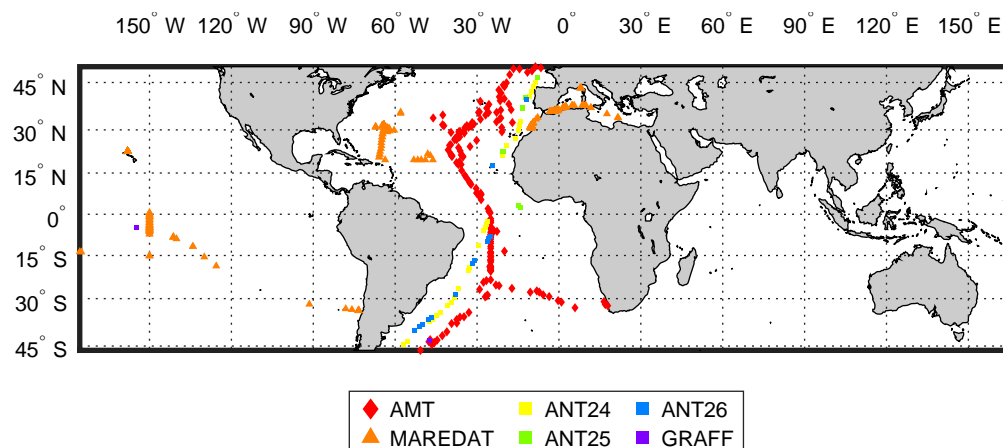
Figure E3. Picophytoplankton Cruises transects
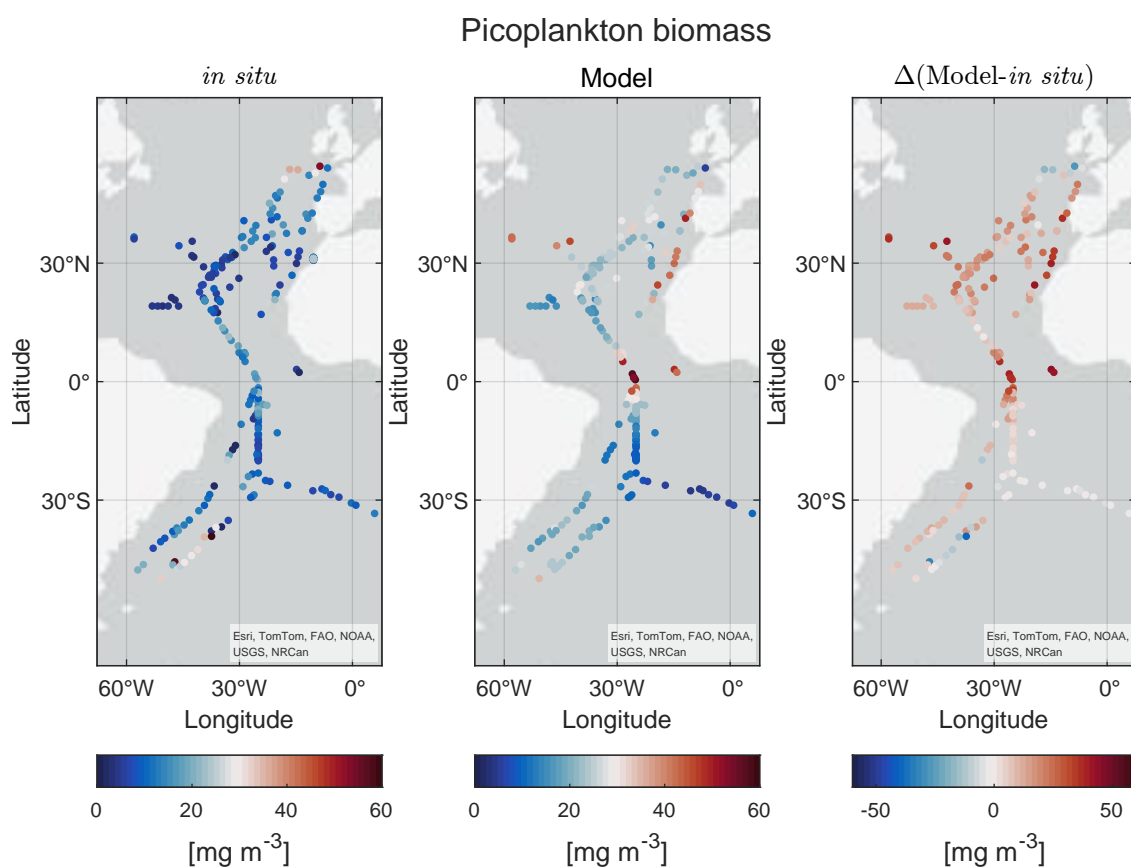
Figure E4. Comparison of picophytoplankton *in situ* data with model picoplankton biomass.
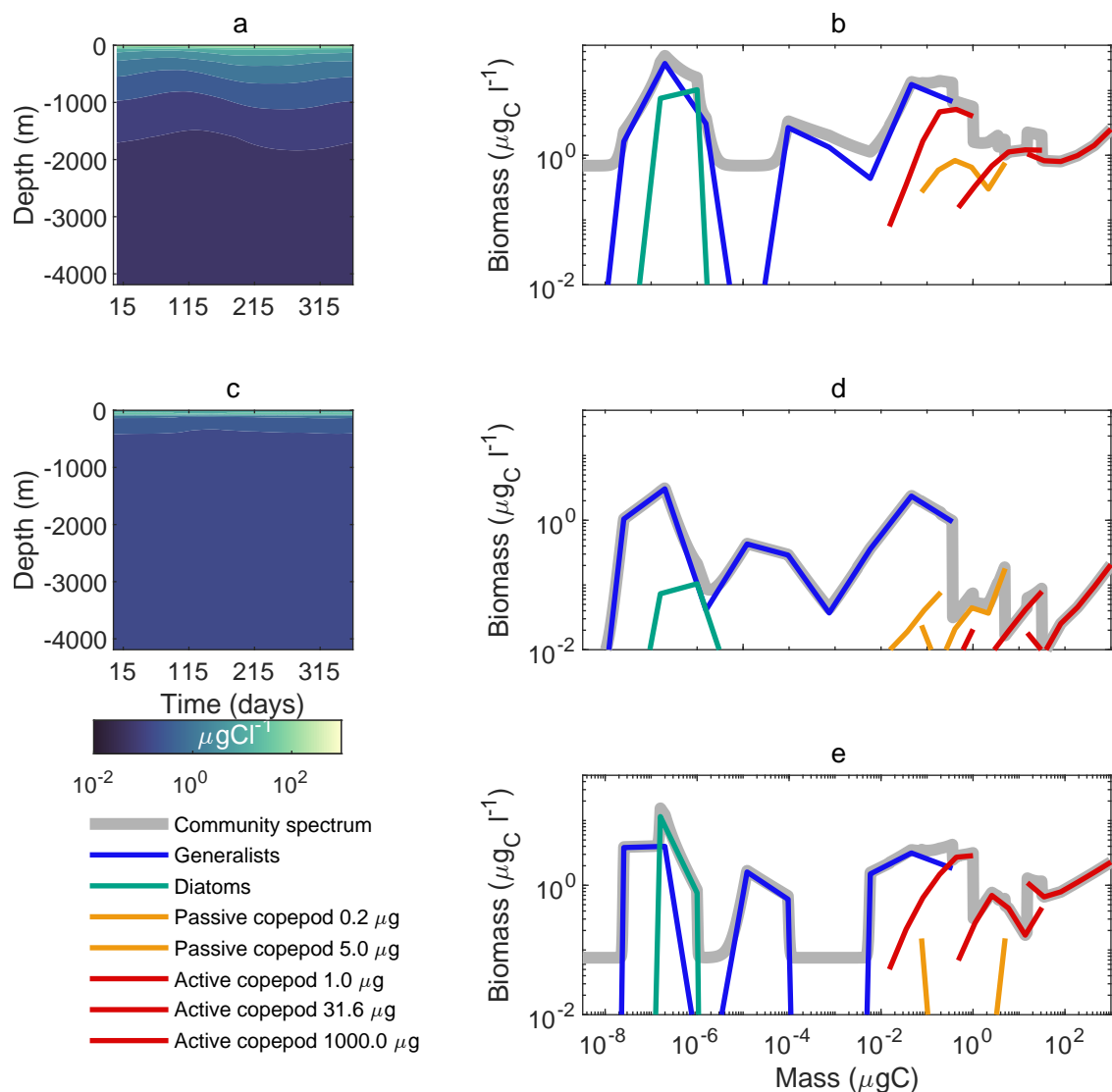
Figure F1. Model output for a 10-year simulation in the global, water column and chemostat model. (a) Total biomass in a water column extracted from the global simulation from Fig. 7 at an upwelling location (5°S, 5°E). (c) Same as (a) but extracted from the watercolumn model. (b),(d),(e): Sheldon spectrum of the community from global, water column and chemostat models at 5 meters depth and averaged over the last year.
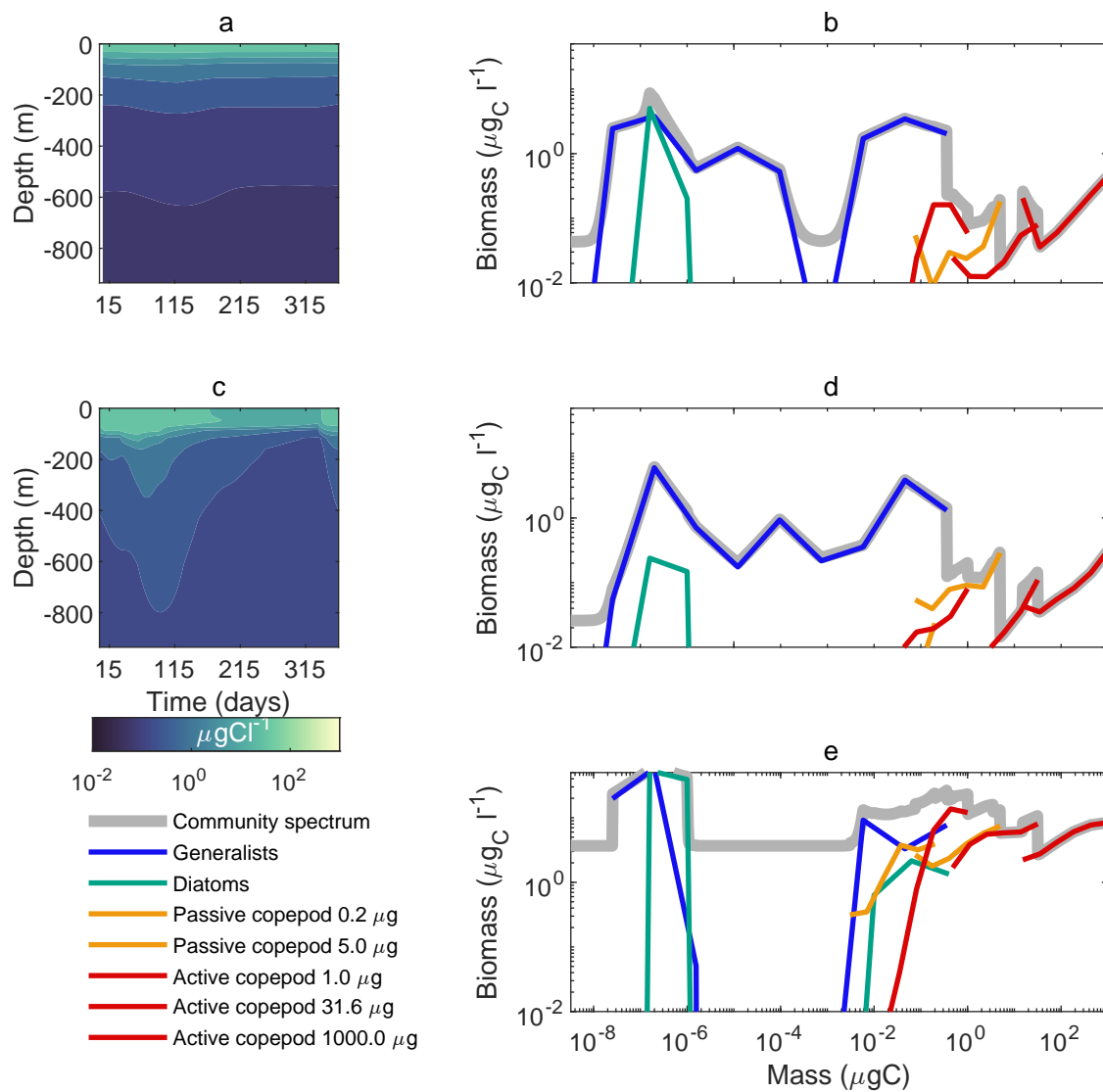
Figure F2. Same as in fig. F1, but at an oligotrophic location (24°N, 158°W).
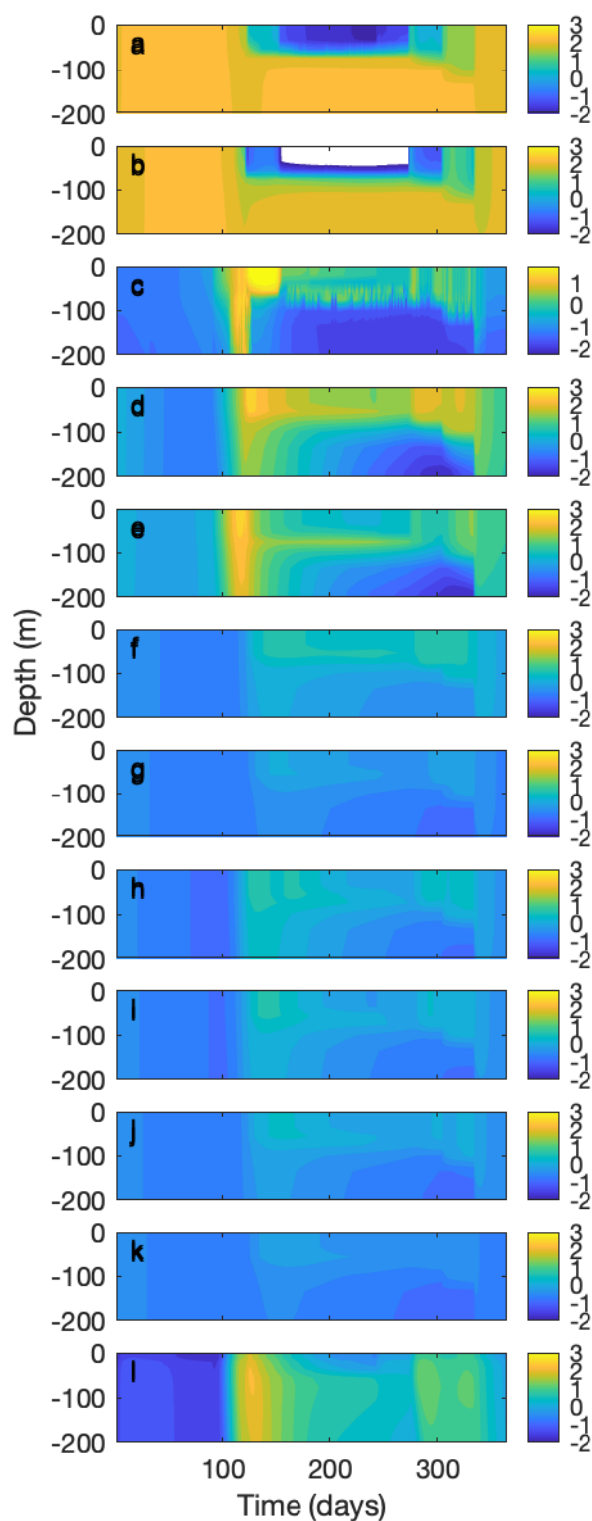
Figure F3. Output of a water-column simulation corresponding to Fig. 14c: (from top to bottom) (a) surface nitrogen ($\mu g_N/l$), (b) silicate ($\mu g_{Si}/l$), and (c) DOC ($\mu g_C/l$); (d) total generalist biomass ($\mu g_C/m^2$), (e) diatom biomass, (f) passive copepod $0.2\,\mu g_C$, (g) passive copepod $5\,\mu g_C$, (h) active copepod $1.0\,\mu g_C$, (i) active copepod $10\,\mu g_C$, (j) active copepod $100\,\mu g_C$, (k) active copepod $1000\,\mu g_C$, and (l) POM. White areas correspond to values lower than 10^{-2}.
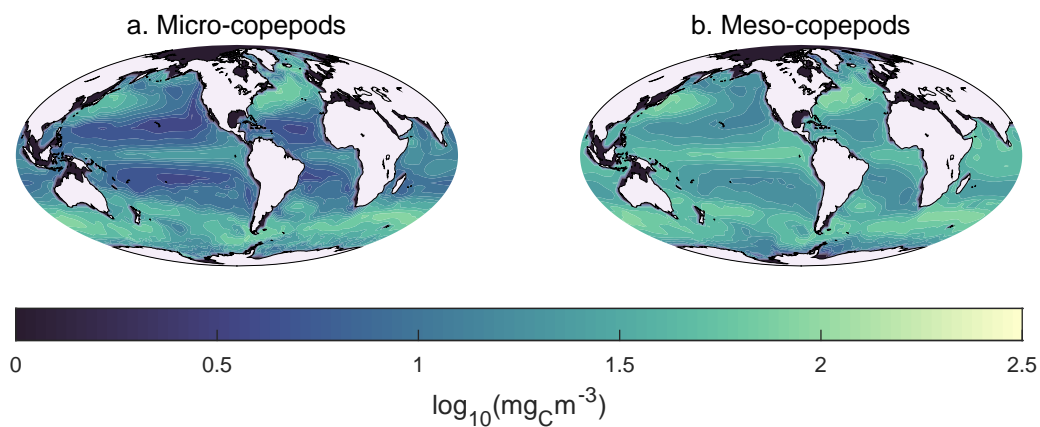
Figure F4. Modeled annual mean micro- and meso-zooplankton biomass of copepods at the top 170m.
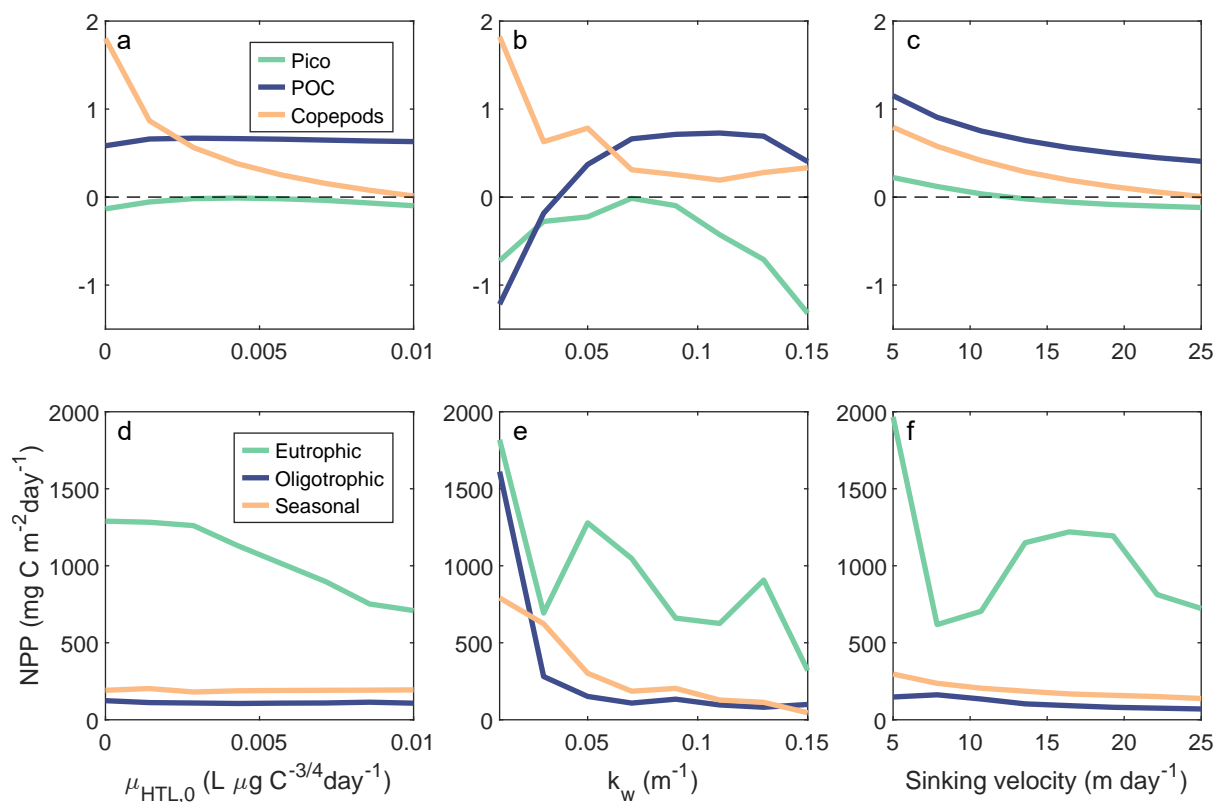
Figure F5. Sensitivity analysis of the parameters μ, k_w and sinking velocity at three characteristic water columns extracted from global simulations
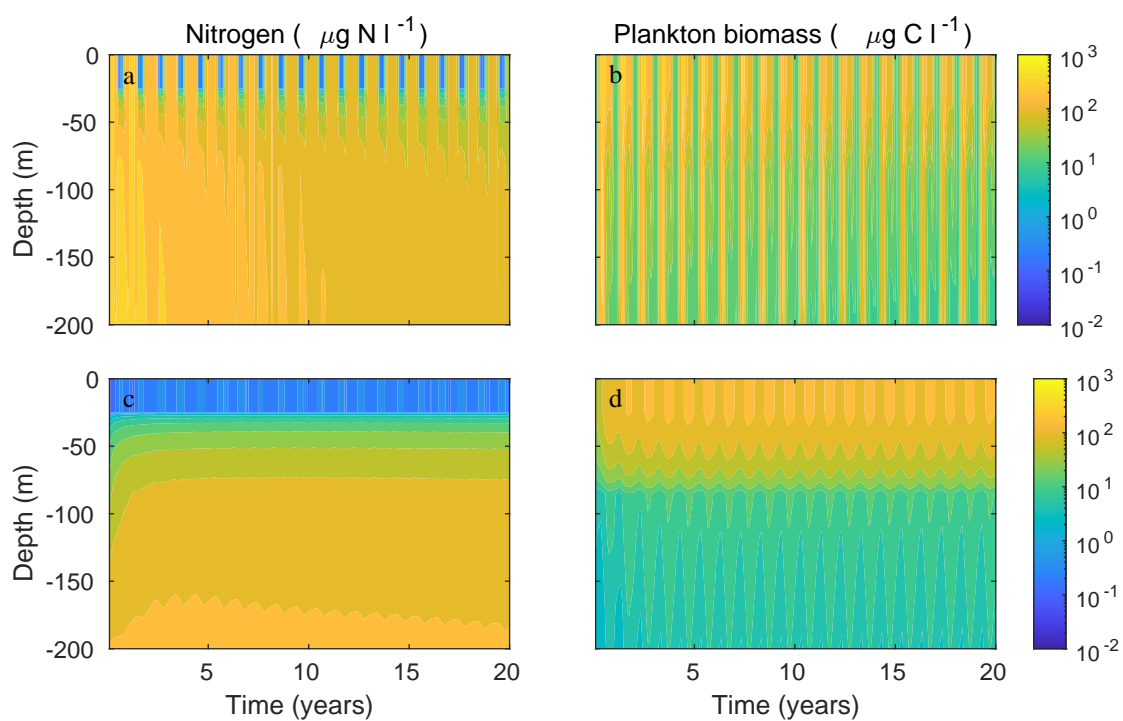
Figure F6. Convergence of a global simulation in a seasonal environment (60°N, 15°W; a,b) and at equator (0°N, 15°W; c,d).